Precambrian Research 237 (2013) 78–100

Contents lists available at ScienceDirect

Precambrian Research

journal homepage: www.elsevier.com/locate/precamres

Geochronology and trace element geochemistry of zircon, monazite and garnet from the garnetite and/or associated other high-grade rocks: Implications for Palaeoproterozoic tectonothermal evolution of the Khondalite Belt, North China Craton

Shujuan Jiao[a,*], Jinghui Guo[a], Simon L. Harley[b], Peng Peng[a]

[a] State Key Laboratory of Lithospheric Evolution, Institute of Geology and Geophysics, Chinese Academy of Sciences, Beijing 100029, China
[b] Grant Institute of Earth Science, School of Geosciences, University of Edinburgh, Edinburgh EH9 3JW, UK

ARTICLE INFO

Article history:
Received 21 January 2013
Received in revised form 29 August 2013
Accepted 7 September 2013
Available online 17 September 2013

Keywords:
Khondalite Belt
Monazite chemical dating
North China Craton
Trace element geochemistry
Zircon U–Pb dating

ABSTRACT

It is well documented that the Khondalite Belt of the North China Craton formed by the collision of the Yinshan and Ordos Blocks during ca. 1.95 Ga, but the onset of the post-collisional exhumation stage has not been well dated. The garnetite and garnet-bearing quartz-rich lens that are regarded as residue-melt phases occur occasionally in the foliated metasedimentary rocks in the Jining terrane of the Khondalite Belt. They are free of regional gneissosity, and may be generated during the post-collisional exhumation stage. Zircon U–Pb dating, monazite chemical dating and trace element analyses of zircon, monazite and garnet have been carried out on the garnetites and associated other high-grade metamorphic rocks. The geochronological results reveal a major age group of ca. 1890 Ma from the zircon grains/overgrowths and inclusion-type monazites within the garnet poikiloblasts in the garnetites. The trace elements analyses show that zircon hosted in the mantle of the garnet poikiloblasts in the garnetite contains the highest HREE and Y contents, whereas zircon hosted in the garnet rims shows higher HREE and Y contents than matrix zircon grains. Inclusion-type monazite in the garnetite shows higher La_N/Sm_N ratio than matrix monazite grains. Large garnet poikiloblasts in the garnetite exhibit bell-shaped HREE and Y zoning profiles attributed to Rayleigh fractionation during their growth. Compared to garnet poikiloblasts, coronal garnet shows higher Gro, Cr and Li contents, but lower X_{Mg}, Sm, HREE, Zn and Zr contents and weaker Eu negative anomalies, reflecting their different formation environments. Based on evidences from microstructural analyses, REE concentrations and patterns, HREE partition coefficients and the Ti-in-zircon thermometer, it is proposed that most of the zircon grains/overgrowths in the garnetite formed coevally with garnet poikiloblasts. Consequently, ca. 1890 Ma represents the timing of garnet poikiloblast growth during the partial melting of the protolith. Coronal garnet or Zn-rich spinel plus cordierite coupled with the matrix-type monazite formed after garnet poikiloblasts growth during near-isothermal decompression. Given the high metamorphic temperature and pressure revealed by the garnetite (820–850 °C and up to 950 °C; 8.5–9.5 kbar), it is suggested that the ca. 1890 Ma age group represents the beginning of extension/exhumation event in the Khondalite Belt, which is also recorded in the associated other high-grade rocks such as the garnet-bearing quartz-rich lenses, sillimanite–garnet-bearing quartzo-feldspathic gneisses, garnet-bearing quartzo-feldspathic gneisses and a pure quartz vein.

1. Introduction

Zircon and monazite are commonly used minerals for U–Pb geochronology, because of their chemical and mechanical stability during the geological events, and ubiquity in both the igneous and metamorphic rocks. The advances in analytical methods, especially the improvement of equipments such as LA-ICP-MS and SIMS, make it possible to measure individual growth zoning of the accessory minerals at high spatial resolution. Monazite chemical (or electron microprobe: EMP) dating is another tool to constrain geochronology (Montel et al., 1996; Braun et al., 1998; Cocherie et al., 1998; Crowley and Ghent, 1999; Cocherie and Albarede, 2001) based on the fact that the monazite contains significant U and Th contents, but negligible common Pb. Monazite chemical dating is able to determine U, Th, and Pb concentrations in domains 2 μm in size, smaller than the smallest possible spot size of LA-ICP-MS.

* Corresponding author. Present address: Institute of Geology and Geophysics, Chinese Academy of Sciences, No. 19, Beitucheng West Road, Chaoyang District, 100029 Beijing, China. Tel.: +86 010 82998521; fax: +86 010 62010846.
E-mail address: jiaoshujuan0215@126.com (S. Jiao).

0301-9268/$ – see front matter © 2013 Elsevier B.V. All rights reserved.
http://dx.doi.org/10.1016/j.precamres.2013.09.008

Both zircon and monazite show high closure temperatures for the U–Th–Pb isotope system and low Pb diffusivity (Cherniak and Watson, 2001; Cherniak et al., 2004), and thus are key to dating events in high-grade metamorphism. However, interpretation of the geochronological data may be ambiguous, particularly in poly-metamorphic terranes. Zircon may either grow during the prograde partial melting, or crystallize from the solidifying melt (Hermann and Rubatto, 2003; Whitehouse and Platt, 2003; Harley et al., 2007; Kelsey and Powell, 2011), or form by decomposition of the Zr-bearing phases such as garnet or ilmenite (Fraser et al., 1997; Degeling et al., 2001; Clark et al., 2009). Similarly, it has been documented that monazite could grow during either prograde or retrograde metamorphic processes, and does not necessarily reflect the timing of peak metamorphism (Hermann and Rubatto, 2003; Fitzsimons et al., 2005; Kelly et al., 2006; Liu et al., 2006). Furthermore, a single monazite may preserve multiple growth zoning due to coupled dissolution–reprecipitation processes, and hence record various apparent ages. As the response the behavior of these two minerals in high-grade metamorphism are complex, and it has become increasingly important to understand the processes through which zircon and monazite have grown or been modified and their abilities of recording the past events in order to better constrain the timing of tectonothermal events (e.g. Harley et al., 2007).

In the Khondalite Belt of the North China Craton extensive geochronological data have been reported in the recent years. These have revealed multiple tectonothermal events including magmatism at 2.56–2.50 Ga, 2.45–2.37 Ga, 2.30–2.00 Ga, 1.96–1.94 Ga, and 1.85–1.82 Ga (mainly in the Daqingshan region), and metamorphic overprints at 1.97–1.94 Ga and 1.87–1.82 Ga (Wu et al., 1998, 2006; Xia et al., 2006a,b, 2008; Wan et al., 2006, 2009, 2013; Yin et al., 2009, 2011; Zhao et al., 2010b; Li et al., 2011; Ma et al., 2012; Dong et al., 2013; Liu et al., 2013). However, it still remains unknown why the metamorphic rocks within the Khondalite Belt encountered and recorded so many magmatic and metamorphic events, especially whether the younger 1.87–1.82 metamorphism was the result of a separate thermal overprint or related to orogenic extension following on from orogenesis at 1.97–1.94 Ga.

In this paper, we have focused on garnetite and associated garnet-bearing quartz-rich lens that are regarded as residue-melt phases with no regional gneissosity. These occur in the high-grade metasedimentary rocks of the Khondalite Belt, and may be generated after the regional continental collision between the Yinshan and Ordos Blocks. Detailed petrography, zircon U–Pb dating, monazite chemical dating, and trace element analyses of accessory and major minerals (i.e. zircon, monazite, and garnet) have been carried out in the garnetites, garnet-bearing quartz-rich lenses and/or their country rocks, such as the garnet-bearing quartzo-feldspathic gneisses, sillimanite–garnet-bearing quartzo-feldspathic gneisses, and a pure quartz vein from the Jining terrane of the Khondalite Belt. Using CL/BSE imaging of the accessory minerals in combination with detailed petrographical and geochemical analyses have enabled zircon and monazite chemical groups to be correlated with garnet growth and hence the obtained ages to be linked with particular *P–T* conditions. The results of this integrated study are used to inform a discussion of the post-collisional tectonothermal evolution of the Khondalite Belt of the North China Craton.

2. Geological setting and sample location

The North China Craton is bounded by the Central Asian Orogenic Belt in the north, the Su–Lu Orogen in the east, the Qinling-Dabie Orogen in the south, and the Qilianshan Orogen in the west, and covers ca. 1.5 million square kilometers (Fig. 1a; Zheng et al., 2013). The basement of the North China Craton has been divided into the Archean to Paleoproterozoic Eastern, Yinshan and Ordos Blocks, and three Paleoproterozoic orogenic belts, namely the Trans-North China Orogen, Khondalite Belt, and Jiao-Liao-Ji Belt (Fig. 1b) (Zhao et al., 2001, 2003, 2005; Zhao and Cawood, 2012; Zhao and Guo, 2012). It is suggested that the North China Craton formed by collision between the Eastern and Western Blocks along the Trans-North China Orogen at ca. 1.85 Ga (Guo et al., 2001, 2005; Zhao et al., 2002, 2006, 2007, 2008a,b, 2010a; Wilde and Zhao, 2005; Kröner et al., 2006; Zhang et al., 2006, 2007, 2009; Lu et al., 2008; Li et al., 2010a,b; Xiao et al., 2011). Before the final collision, the Western Block formed by amalgamation of the Ordos and Yinshan Blocks along the east-west-trending Khondalite Belt at ca. 1.95 Ga (Zhao et al., 2005, 2010b; Yin et al., 2009, 2011; Santosh, 2010). Recently, Zhao and Zhai (2013) have suggested that the boundary between the Khondalite Belt and the Ordos Block might be refined based on the new borehole data that reveal the Paleoproterozoic rocks in the western and eastern margins of the Ordos Block, which are similar to those in the Khondalite Belt (Hu et al., 2013).

The Khondalite Belt in the Western Block is divisible into three terranes from west to east: Helanshan-Qianlishan (HL-QL), Daqingshan-Ulashan (DU) and Jining (JN) (Fig. 1b), which are predominated by quartzo-feldspathic gneisses, graphite-bearing garnet-sillimanite gneisses, feldspathic garnet quartzites, marbles and calc-silicate rocks (Condie et al., 1992; Lu et al., 1992, 1996; Zhao et al., 1999, 2005). There are also minor TTG gneisses, mafic granulites, charnockites and S-type granites in association with the predominant metasedimentary rocks. Moreover, several localities with ultrahigh-temperature (UHT) assemblages have recently been recognized in the Khondalite Belt, mainly situated in the eastern Daqingshan-Ulashan terrane (e.g. Dongpo) and the central Jining terrane (e.g. Tuguiwula) (e.g. Santosh et al., 2006, 2007a,b; Tsunogae et al., 2011; Guo et al., 2012).

The Jining terrane is close to the junction of the Khondalite Belt and the Trans-North China Orogen (Fig. 2; Zhao et al., 2005), where representative lithologies are granulite-facies sillimanite–garnet-K-feldspar gneisses and quartzo-feldspathic gneisses that contain horizons of marble, calc-magnesium silicate rocks, mafic granulite and rare graphitic gneiss, as well as extensive S-type granites and charnockites that are particularly abundant in the southwest Jining terrane (Liangcheng area) (Lu et al., 1992). Gabbroic and noritic to dioritic intrusive bodies are also common, and have undergone high-temperature granulite-facies metamorphism, especially in the Xuwujia area (Peng et al., 2010).

Most of samples for this study were collected from the Dashizi-Xiaoshizi area in the Jining terrane (Fig. 2). This area is dominated by metasandstones and metagreywackes, such as quartzo-feldspathic sillimanite–garnet gneisses, garnet-biotite arkosic quartzites, fine-grained quartzo-feldspathic gneisses, and minor fine-grained microcline-biotite gneisses, sillimanite–garnet quartzites and arkosic quartzites. The metasandstones and metagreywackes define a tight fold with a NE-SW axial direction (Fig. 3). Garnet-bearing granites occur in the southern part of the area, whereas charnockites are located in the northern part (Fig. 3). Minor mafic granulites have been emplaced into charnockites, and occur as lenses (Fig. 3). Marble horizons occur between the charnockites and metagreywackes near a ductile high-strain zone. Post-folding and strike-slip faults are widely developed in this area. Garnetites (samples 11XSZ01, 09DSZ20, 20′) and associated garnet-bearing quartz-rich lenses (samples 11XSZ0203) develop as an irregular pod (ca. 7 m long, ca. 5 m wide) within the sillimanite–garnet-bearing quartzo-feldspathic gneisses (samples 11XSZ04, 06) on a small hill close to Xiaoshizi Village (Location A in Fig. 3). Pure quartz veins (sample 11XSZ07) occur on an adjacent

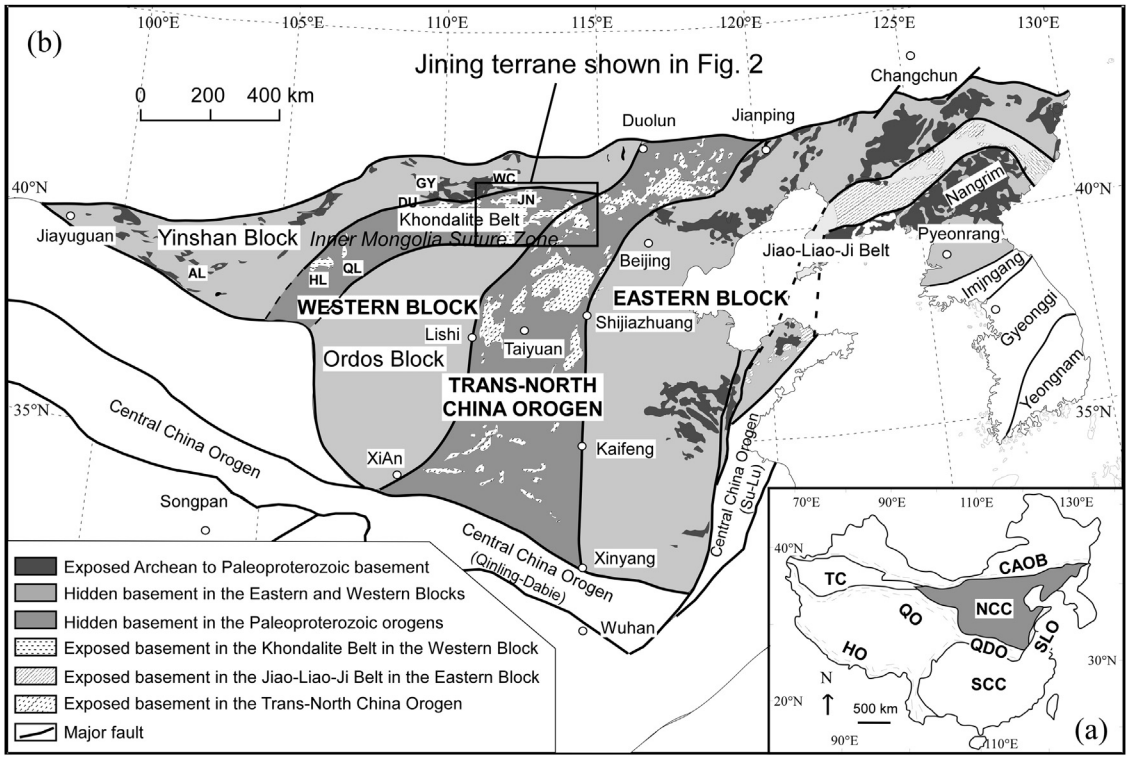

Fig. 1. (a). Tectonic map of China showing major cratons and orogens (after Zhao et al., 2001). (b). Geological and tectonic map of the North China Craton (after Zhao et al., 2005). Abbreviations of areas: CAOB, Central Asian Orogenic Belt; HO, Himalaya Orogen; NCC, North China Craton; SCC, South China Craton; SLO, Su-Lu Orogen; TC, Tarim Craton; QDO, Qinling-Dabie Orogen; QO, Qilianshan Orogen. Abbreviations of metamorphic complexes: AL, Alashan. DU, Daqingshan-Ulashan; GY, Guyang; HL, Helanshan; JN, Jining; QL, Qianlishan; WC, Wuchuan.

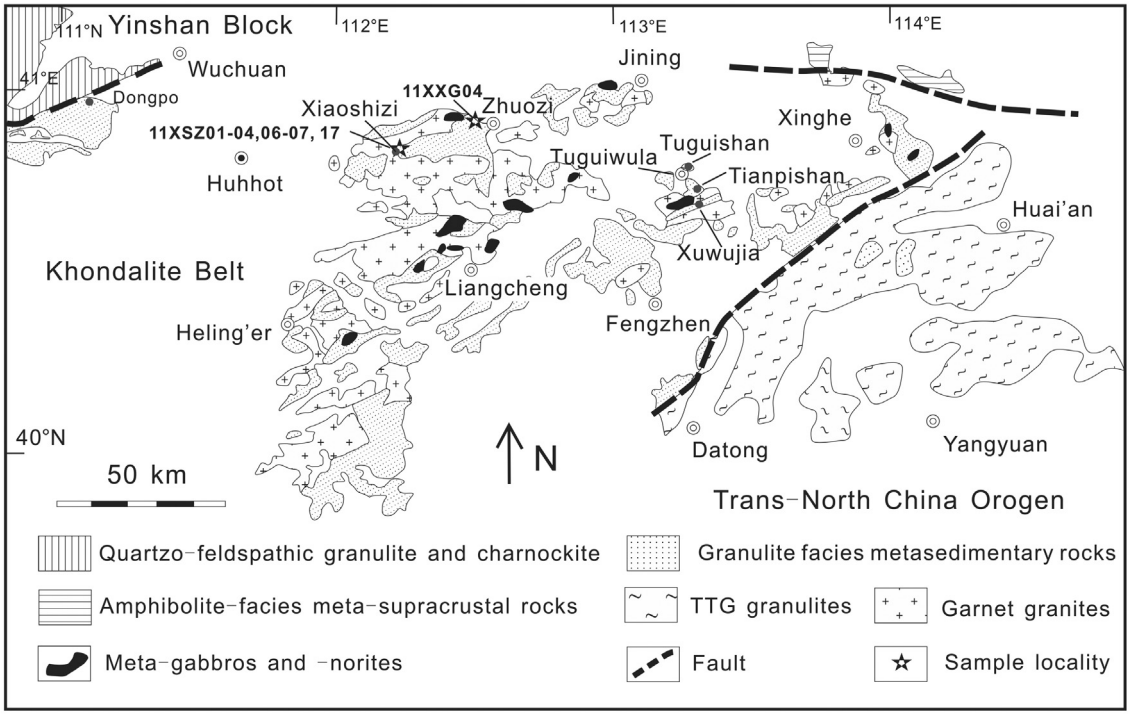

Fig. 2. Distribution of the high-grade metamorphic rocks in the eastern segment of the Khondalite Belt, North China Craton. Modified after Guo et al. (2001).

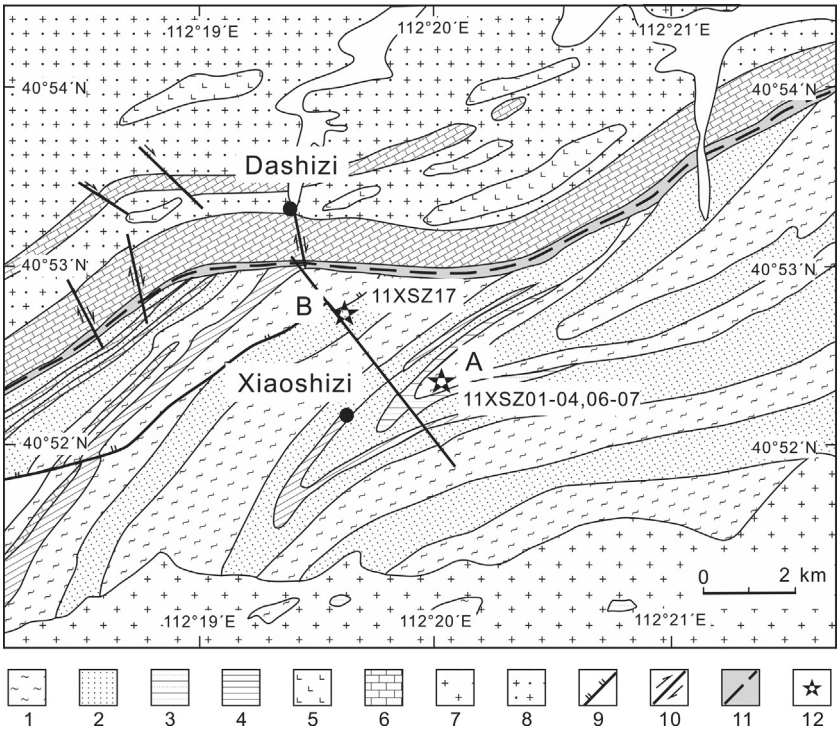

Fig. 3. A local geological map of the Dashizi and Xiaoshizi areas (modified after Lu et al., 1992). (1) Quartzo-feldspathic sillimanite–garnet gneiss, (2) Garnet-biotite arkosic quartzite and fine-grained quartzo-feldspathic gneiss, (3) fine-grained microcline-biotite gneiss, (4) sillimanite–garnet quartzite and arkosic quartzite, (5) mafic granulite, (6) marble, (7) garnet-bearing granite, (8) charnockite, (9) thrust fault, (10) strike-slip fault, (11) ductile deformation zone, and (12) sample location.

hill. Garnet-bearing quartzo-feldspathic gneiss (sample 11XSZ17) was collected at location B in Fig. 3. Sample 11XXG04, a garnet-bearing quartzo-feldspathic gneiss, was sampled along the No. 110 national road from Zhuozi to Huhhot close to Xiaoxigou Village (Fig. 2). Representative field photographs are referred to Fig. 4 in Jiao et al. (2013).

3. Metamorphism and sample description

3.1. Metamorphism of the garnetite

The garnetite consists of >60 vol% garnet (Fig. 4a), accompanied by sillimanite and quartz (Fig. 4b–d) associated with minor plagioclase, biotite, cordierite, spinel, orthopyroxene and other accessory minerals such as ilmenite, rutile, zircon and monazite. No foliation has been identified. Garnet poikiloblasts show varying degrees of resorption and reaction texture in different microdomains (Fig. 4c–e). The microdomainal mineral assemblages of the garnetite have been studied in a separate paper and are summarized as follows (Jiao et al., 2013). Garnet poikiloblasts (Grt1) coupled with the inclusion and matrix minerals involving quartz, sillimanite, plagioclase, biotite, rutile and ilmenite define the peak metamorphic stage M1, with *P–T* conditions of 820–850 °C (and rarely up to 950 °C based on Zr-in-rutile thermometer) and 8.5–9.5 kbar. Post-peak reactions between garnet and sillimanite with or without quartz resulted in the formation of Grt2 + Crd (M2a) or Spl + Crd (M2b) assemblages (Fig. 4c and d), respectively, and *P–T* conditions of M2 are 850–865 °C and 7.4–7.6 kbar. The final stage (M3) is represented by the Opx + Crd + Pl + Grt3 + Bt assemblage formed surrounding garnet (Fig. 4e) at *P–T* conditions of 710–720 °C and 6.4–6.6 kbar. These results are consistent with a clockwise *P–T* path predominated by near-isothermal decompression and subsequent cooling and decompression, interpreted to reflect the extension and exhumation of the Khondalite Belt after the continental collision between the Yinshan and Ordos Blocks. It is suggested that the garnetite and associated garnet-bearing quartz-rich lens are the residuum after the partial melting and K, Na-rich melt extraction during or after the formation of peritectic garnet poikiloblasts (Jiao et al., 2013). Mineral abbreviations are referred to Whitney and Evans (2010).

3.2. Sample description

Samples 11XSZ01, 09DSZ20, and 09DSZ20′ are garnetites, which have been described above. Zircons in these samples are generally present in three distinct settings: (a) as round- or elliptically shaped inclusions in the mantle/rim of garnet poikiloblasts (Fig. 5a), or in contact with/surrounding garnet rim or sillimanite (Fig. 5b, d–i), (b) in the core of garnet poikiloblast associated with monazite, rutile and plagioclase (Fig. 5c), and (c) as irregularly shaped grains present in association with ilmenite in the matrix (Fig. 5j). Fig. 5c shows a comparison of zircon grains (a) and (b), while Fig. 5j shows a comparison of zircon grains (a) and (c). Monazites are present in two distinct textural settings: (a) as inclusions in garnet poikiloblasts and coexisting with zircon, rutile and occasional plagioclase (Fig. 6a and b), and (b) surrounding ilmenite (Fig. 6c), or sillimanite (Fig. 6d) in the matrix. Monazite is variable from round to irregular in shape (Fig. 6), with the inclusion-type monazite preserving a more regular shape than the matrix monazites.

Samples 11XSZ02 and 11XSZ03 were collected from the garnet-bearing quartz-rich lenses (Fig. 4f). Sample 11XSZ02 is composed of 90% quartz, 7% garnet, 1–2% biotite and minor accessory rutile, zircon and monazite. Garnet is subhedral–euhedral (0.5–2.0 mm), contains few or no quartz inclusions, and may be replaced by biotite on its rim. No foliation is observed. Zircon is generally enclosed in quartz in the matrix. Sample 11XSZ03 consists of 90% quartz, less abundant garnet (5%), 1–2% biotite and minor K-feldspar as well as zircon and monazite. Garnet is smaller with a

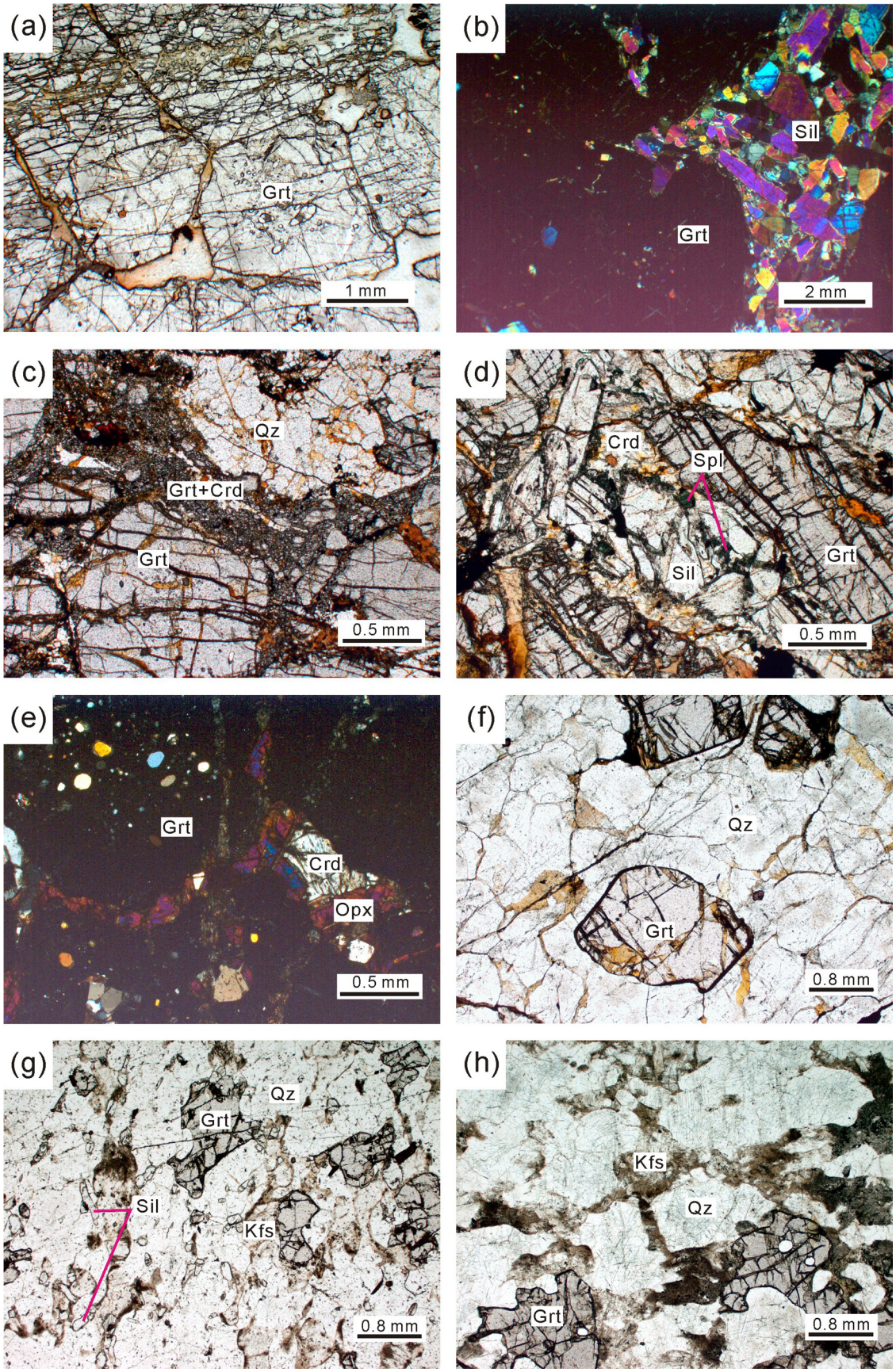

Fig. 4. Photomicrographs showing mineral associations of the collected samples. (a) Garnetite that consists of >60 vol% garnets; (b) garnetite showing coexistence of garnet and sillimanite; (c) Grt + Crd corona around the large garnet poikiloblast in garnetite; (d) Spl + Crd symplectite between sillimanite and garnet in garnetite; (e) orthopyroxene associated with cordierite and/or plagioclase around garnet in garnetite; (f) garnet-bearing quartz-rich lens; (g) sillimanite–garnet-bearing quartzo-feldspathic gneiss; and (h) garnet-bearing quartzo-feldspathic gneiss.

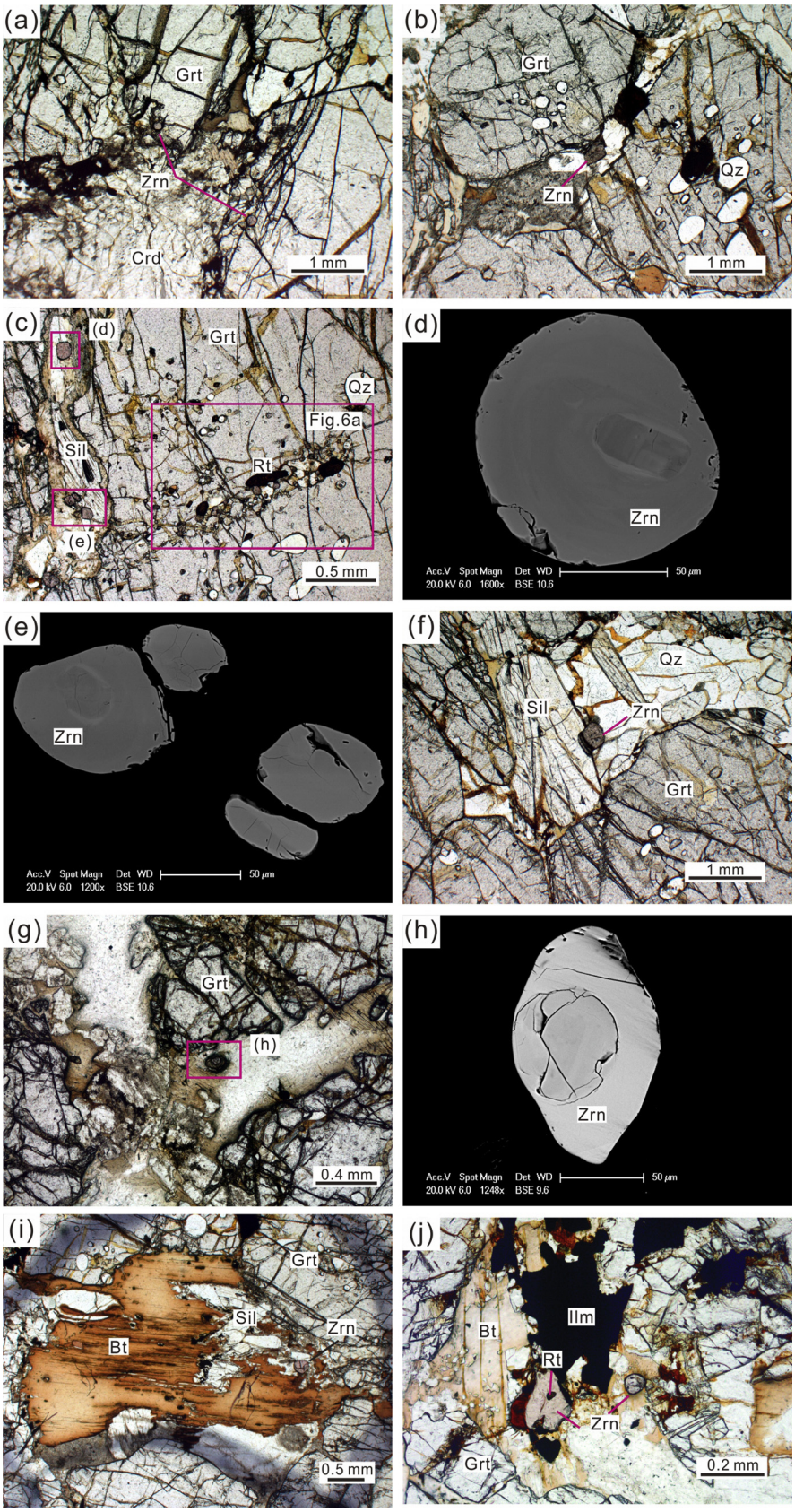

Fig. 5. Photomicrographs and back-scattered electron images showing localities of zircon grains in the garnetite. (a) Zircon grains in the rim of garnet; (b) zircon grain contacting with the rim of garnet in matrix; (c) parts of zircon grains growing outside garnet and contacting with sillimanite, and the other growing inside garnet and contacting with rutile and monazite; (d–e) BSE imaging of zircon grains occurring in Fig. 5c, which show distinct core–rim or homogeneous unzoned feature; (f) zircon growing between sillimanite and quartz in matrix; (g) zircon grain growing around garnet in matrix; (h) BSE imaging of zircon occurring in Fig. 5g, with a distinct core–rim structure; (i) zircon grain occurring between biotite and sillimanite in matrix; and (j) an anhedral irregular zircon grain growing after ilmenite, but another euhedral grain keeping away from it in matrix.

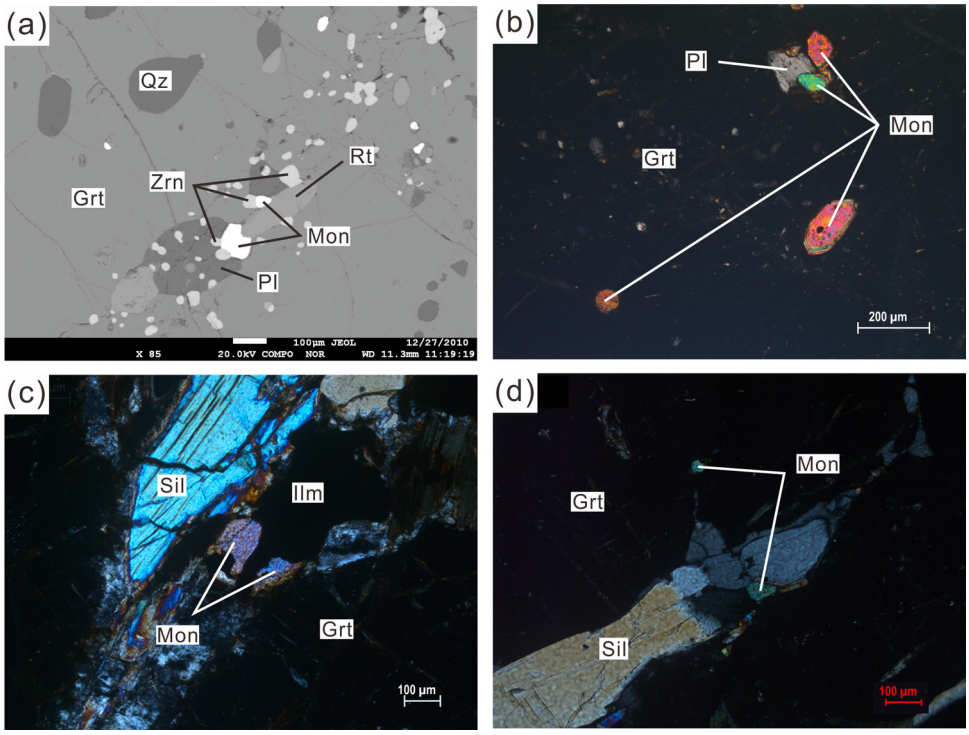

Fig. 6. Photomicrographs and back-scattered electron images showing localities of monazite grains in the garnetite. (a) Monazite grains occurring as inclusions in garnet, associated with zircon, rutile and plagioclase; (b) monazite grains as inclusions in garnet; (c) monazite grains associated with ilmenite between sillimanite and garnet in matrix; and (d) a monazite grain occurring in the mantle of garnet, another grain growing with sillimanite in matrix.

diameter of 0.2–1.2 mm, contains no inclusions, and is occasionally replaced by biotite. Zircon is generally present in quartz in the matrix.

Samples 11XSZ04 and 11XSZ06 are sillimanite–garnet-bearing quartzo-feldspathic gneisses (Fig. 4g). Sample 11XSZ04 is composed of 70% quartz, 10% plagioclase, 5% sillimanite, 5% garnet, 5% K-feldspar and minor accessory minerals such as rutile, ilmenite, zircon and monazite. Garnet porphyroblasts are anhedral–subhedral (0.1–1.0 mm), and contains rare quartz inclusions. A weak foliation is defined by the orientation of the prismatic sillimanites. Zircon is generally situated in the matrix. Sample 11XSZ06 consists of 60% quartz, 20% perthite, 7% garnet, 5% sillimanite, 2% plagioclase and minor rutile, zircon and monazite. Garnet porphyroblasts are larger with diameters of 0.5–2 mm, and shows a poikiloblastic structure with quartz and plagioclase as inclusions. Prismatic sillimanite crystals are oriented to form a weak foliation. Zircon mainly appears in the matrix.

Sample 11XSZ07 was collected from a pure quartz vein, which contains nearly 99% quartz and minor zircon and monazite.

Samples 11XSZ17 and 11XXG04 are garnet-bearing quartzo-feldspathic gneisses (Fig. 4h), of which sample 11XSZ17 consists of 70% quartz, 10% K-feldspar, 10% plagioclase, 7% garnet and minor muscovite and accessory minerals such as rutile, ilmenite, zircon and monazite. Garnet porphyroblasts are subhedral–anhedral (0.2–1.0 mm), contain rare quartz inclusions. Zircon is present in the matrix. Sample 11XXG04 consists of 70% quartz, 15% garnet, 10% perthite, 2% rutile, 1–2% mica with minor zircon and monazite. Garnet porphyroblasts vary from 0.5 mm to 1.5 cm in diameter. The largest garnet grains are subhedral–anhedral, strongly corroded and diablastic, and enclose quartz inclusions, whereas the smaller garnets usually occur between intergranular quartz grains and show irregular shapes. Perthite is generally entirely replaced by sericite. The orientation of biotite and muscovite coupled with sericitized perthite defines a foliation. Zircon is mainly present in the matrix.

4. Analytical method

4.1. Sample preparation

Samples were crushed to select zircon grains by conventional density and magnetic techniques. The selected zircon grains together with zircon standards 91500 were mounted in epoxy mounts which were then polished to section the crystals in half for analysis. The structures and inclusions of zircon grains were documented with transmitted and reflected light micrographs, and cathodoluminescence (CL) imaging that was carried out using a LEO1450VP scanning electron microscope (SEM) with a MiniCL Cathodoluminescence system at the Institute of Geology and Geophysics, Chinese Academy of Sciences. An accelerating voltage of 15 kV, a beam current of 1.1 nA, and a work distance of 27–29 mm were used during the analyses. Inclusions in zircons were analyzed by Laser Raman Spectroscopy (RE 1000) at the Institute of Geology, Chinese Academy of Geological Sciences. Laser frequency was 514 nm. The mount was vacuum-coated with high-purity gold prior to secondary ion mass spectronmetry (SIMS) analysis.

Monazite was analyzed in situ using standard polished thin sections. Backscattered electron (BSE) imaging of monazite grains was performed using a Philips XL30CP SEM at the School of Geosciences, University of Edinburgh. The analyses were operated at an accelerating voltage of 20 kV, a beam current of 1.5–2.0 nA, and a work distance of 10 mm.

4.2. Zircon U–Pb dating by SIMS

Measurements of U, Th and Pb isotopes were conducted using the Cameca IMS-1280 SIMS at the Institute of Geology and Geophysics, Chinese Academy of Sciences. U–Th–Pb ratios and absolute abundances were determined relative to the standard zircon 91500 (Wiedenbeck et al., 1995), analyses of which were interspersed with those of unknown grains, using data processing procedures

similar to those described by Li et al. (2009). During the analysis, a beam size of 20 μm × 30 μm was used. A long-term uncertainty of 1.5% (1 RSD) for $^{206}Pb/^{238}U$ measurements of the standard zircons was propagated to the unknowns (Li et al., 2010a,b), despite that the measured $^{206}Pb/^{238}U$ error in a specific session was generally around 1% (1 RSD) or less. Measured compositions were corrected for common Pb using non-radiogenic ^{204}Pb. Corrections were sufficiently small to be insensitive to the choice of common Pb composition, and an average of present-day crustal composition (Stacey and Kramers, 1975) was used for the common Pb assuming that the common Pb was largely surface contamination introduced during sample preparation. Uncertainties on individual analyses in data (Supplementary Table 1) were reported at a 1σ level, and mean ages for pooled U/Pb (and Pb/Pb) analyses were quoted with 95% confidence interval. Data reduction was carried out using the Isoplot/Ex v. 2.49 programs (Ludwig, 2001).

4.3. Zircon U–Pb dating (and selected trace element concentration analyses) by LA-ICP-MS

Measurements of U, Th and Pb isotopes and selected trace elements in zircon grains were conducted by Laser Ablation Inductively Coupled Plasma Mass Spectrometry (LA-ICP-MS) at Ministry of Education Key Laboratory of Orogenic Belt and Crustal Evolution, Peking University. The instrument consists of a Lambda Physik ComPex 102 ArF^+ laser (193 nm), and an Agilent 7500ce ICP-MS, connected with a MicroLas GeoLs 200 M optical system. During the analysis, a beam size of 32 μm and a pulse rate of 5 Hz were used, and the produced energy density was 15 J/cm^3. Standard zircon Plesovice was analyzed in order to correct zircon U–Pb ages. NIST 610 glass was used as external standards for the trace element compositions with recommended values taken from Pearce et al. (1997). The isotope ratios and element concentrations were calculated with the "GLITTER" software with dwell-times of 10–50 ms. Analytical results are listed in Supplementary Tables 2 and 4.

4.4. Monazite chemical dating

Electron microprobe (EMP) analysis of monazites was carried out using a 5 spectrometer Camebax SX-100 electron microprobe at the EMMAC, University of Edinburgh following the approach of D. A. Steele (Kelsey et al., 2003; Berry et al., 2007). Monazite analysis was conducted at an accelerating voltage of 20 kV and two beam current conditions – 40 nA for the elements Th (Mα), P (Kα), La (Lα), Ce (Lα) and Nd (Lβ), and 100 nA for the elements U (Mβ), Si (Kα), Pb (Mβ), Ca (Kα), Y (Lα), Pr (Lβ), Sm (Lβ), Gd (Lβ) and Dy (Lβ). Pb was analyzed on two LPET spectrometers, each for 250 s on peak and 150 s on background, leading to detection limits of 100–110 ppm. Analysis time for U was 180 s on peak and 120 on background, yielding a detection limit of 190–200 ppm. All other major elements were analyzed for 20 s on peak (Th, P, La, Ce, Nd) and the remaining elements for 30 s (Pr, Sm), 40 s (Ca, Y), 50 s (Gd), 60 s (Si) and 90 s (Dy). Beam size was set to 8 μm, which results in a physical beam dimension of about 5 μm.

Standards used for peak calibration were Th-oxide (87.88 wt% Th), for Th, $ScPO_4$ (22.14 wt% P) for P, REE (and Y) phosphates for each of La, Ce, Nd, Pr, Sm, Gd, Dy and Y, wollastonite for Ca, Pb-bearing glass K227 (composition: 74.264 wt% Pb; 9.35 wt% Si) for Pb and Si, and pure depleted UO_2 (88.15 wt% U) for U. The magnitude of the ThMα-on-UMβ correction was determined from measurement of apparent U in 10 repeat analyses of the Th-oxide standard, and that of the U-on-PbMβ correction from 10 repeat analyses of the UO_2 standard. The CeLα-on-PbMβ interference, determined by 20 repeat analyses on the Ce-oxide standard, was found to be negligible for the instrumental conditions used. The Moachir monazite secondary standard (J.M. Montel; age 506 ± 6 Ma via TIMS) was analyzed, in sets of 5–10 repeat analyses, before, during and after the analytical session, so that the unknowns were bracketed by 45 analyses of the Moachir monazite. For the analytical session the average age obtained for Moachir was 506.0 ± 5.2 Ma (standard error of the mean, 45 analyses, MSWD 0.47). Monazite chemical ages for each analysis point were processed in an Excel sheet developed at the University of Tasmania by R. F. Berry, with minor modifications by D. A. Steele. According to this procedure, the calculated detection limit (1σ) of the monazite ages is ≤35 Ma (Supplementary Table 3).

4.5. Major element analyses by EMP

Major element compositions of garnet were determined on a JEOL JXA-8230 EMP at the Institute of Mineral Resources, Chinese Academy of Geological Sciences in Beijing, China. Operating conditions were 15 kV for accelerating voltage and 20 nA for beam current with a 1 or 5 μm beam size. Count times were 10 s on peaks, and 5 s on each background. Natural and synthetic phases were used as standards. Minerals were routinely analyzed for Na, Mg, Al, Si, K, Ca, Ti, Mn, Fe, Cr, and Ni. The data were processed with an online ZAF-type correction. The analytical results are listed in Supplementary Table 6.

4.6. Trace element analyses by LA-ICP-MS

Measurements of the trace element compositions of garnets and minor zircon and monazite grains are processed in polished thin sections by LA-ICP-MS at the Institute of Geology and Geophysics, Chinese Academy of Sciences. The instrument is an Agilent 7500a Q-ICP-MS acquired with a 193 nm Lambda Physics Excimer laser (Compex 102). During the experiment, the acceleration voltage was set to be 26 kV and the pulse rate was 8 Hz, yielding an energy density of ca. 10 J/cm^2. NIST 610 glass was used as an external standard with recommended values taken from Pearce et al. (1997). Diameter of the beam spot was 60–30 μm. During analyses of garnet, signals of REE, Ti and Zr were monitored to check contamination of monazite, Ti-bearing phase and zircon inclusions. Element concentrations were calculated with the software "GLITTER". Internal standards of garnet and monazite were Si and Ce, respectively, based on their EMP data, and that of zircon was stoichiometric Si from $ZrSiO_4$. The analytical results are listed in Supplementary Tables 4, 5 and 7.

5. Morphology and geochronology

5.1. Morphology and geochronology of zircon

Zircon grains in all the collected samples are brownish and 60–150 μm in size except sample 11XSZ07 where the grains are a bit larger, even up to 500 μm. Most of the selected grains are subhedral–euhedral and isometric (round or elliptical) or elongated in shape. Zircon crystals (except sample 11XSZ07 where zircons rarely contain inclusions) generally develop cracks and contain abundant inclusions, such as quartz, apatite, rutile, monazite, calcite, sillimanite, plagioclase and CO_2 in sample 11XSZ01 (garnetite). Fig. 7 exhibits the coexistence of gahnite and quartz enclosed by zircon from sample 11XSZ01. CL imaging shows that the round-elliptical grains display core–rim texture involving irregular bright or dark oscillatory-zoned inherited cores which are magmatic component and thin isometric homogenous, structureless medium-gray cathodoluminescent overgrowths. Alternatively, numerous round-elliptical grains show homogeneous unzoned characteristic and display a weakly polygonal sectors without detrital core (Fig. 8). Most of the elongated grains are detrital, and might originate from a magmatic provenance because of the well preserved oscillatory-zoning.

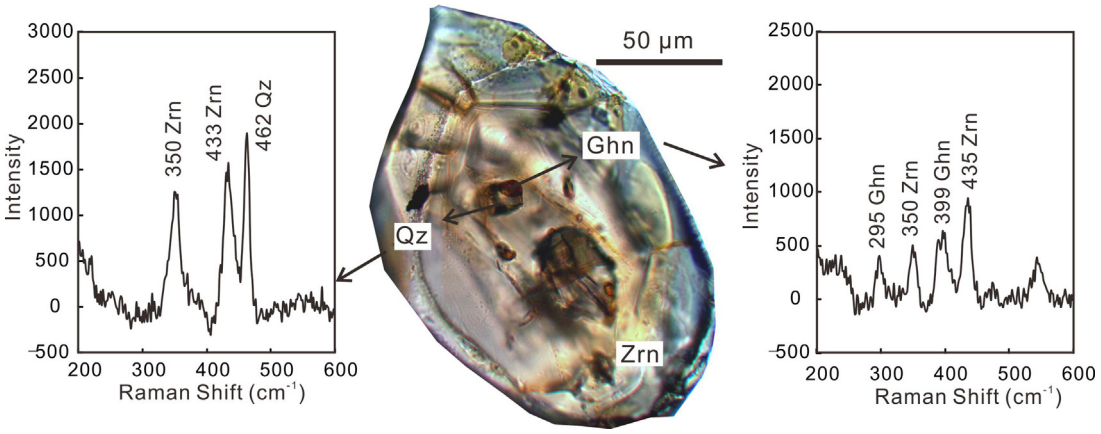

Fig. 7. Laser Raman measurement showing coexistence of quartz and gahnite as inclusions in zircon from garnetite.

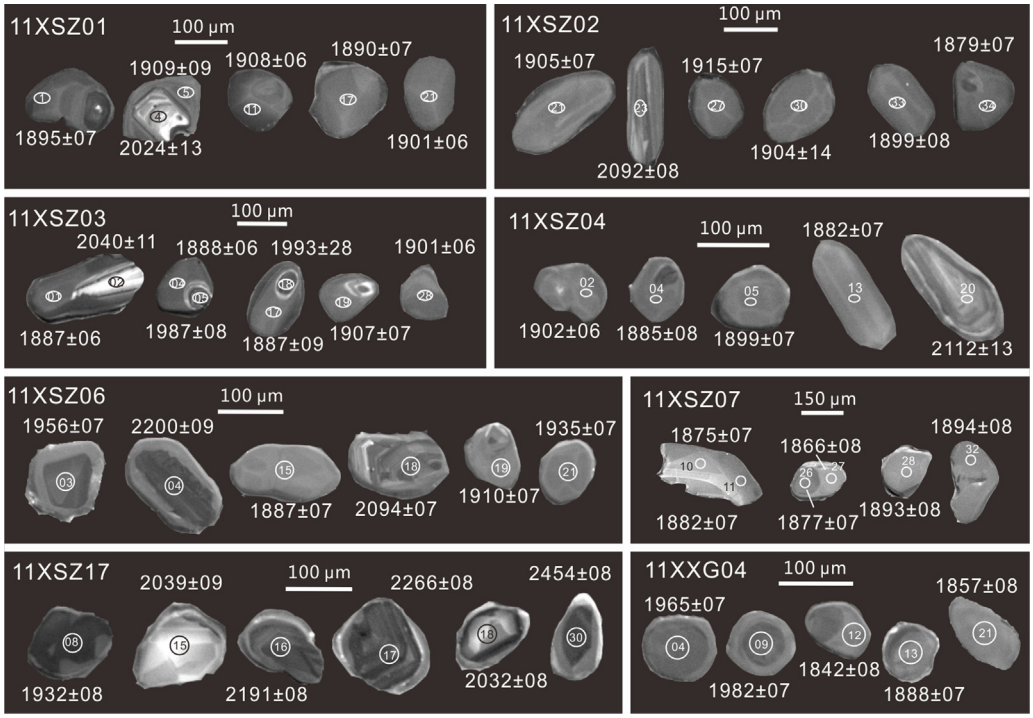

Fig. 8. Cathodoluminescence (CL) imaging of zircon grains from the collected samples, showing the apparent U–Pb ages and analyzed numbers.

Zircon grains selected from samples 11XSZ01-04 were measured by SIMS, and those from samples 11XSZ06-07, -17, 11XXG04 by LA-ICP-MS. The measurements were concentrated on overgrowth of the crystal or the homogeneous unzoned grain, which is more likely to have formed during metamorphism (maybe melt-related). However, for samples 11XSZ06, -17, the majority of zircon crystals are columnar detrital grains, which are difficult to constrain the metamorphic event, but they supply with the provenance information. The detected results are plotted in Figs. 9 and 10, and summarized in Table 1 that focuses on the homogeneous unzoned zircon overgrowths and grains.

5.1.1. Sample 11XSZ01

Twenty-four spots were analyzed on sample 11XSZ01, but four discordant spots were excluded from further calculation (Supplementary Table 1). Three detrital zircon cores and elongated crystals (cores/grains) yield concordia or nearly concordia ages which are 2024 ± 13 Ma, 2069 ± 29 Ma, and 2085 ± 33 Ma (Fig. 9a). The remaining homogeneous unzoned zircon overgrowths and crystals (overgrowths/grains) yield a concordant weighted mean $^{207}Pb/^{206}Pb$ age of 1892 ± 4 Ma (MSWD = 1.7; Fig. 9a).

Three detrital cores/grains have Th contents of 19–107 ppm, U contents of 183–479 ppm, and Th/U ratio of 0.09–0.59. The unzoned overgrowths/grains show Th contents of 37–254 ppm, U contents of 104–1076 ppm, and Th/U ratio of 0.05–0.69.

5.1.2. Sample 11XSZ02

Twenty-six spots were analyzed by SIMS, but three discordant spots were excluded from further calculation (Supplementary Table 1). Three detrital zircon cores/grains yield older ages with one concordia age of 2148 ± 10 Ma compared to the other two detrital cores/grains with one concordia age of 2077 ± 11 Ma (Fig. 9b). The remaining unzoned overgrowths/grains obtain two concordant weighted mean $^{207}Pb/^{206}Pb$ ages of 1916 ± 6 Ma (MSWD = 0.3, N = 4) and 1896 ± 4 Ma (MSWD = 0.2; N = 14; Fig. 9b). However, the grains that yield these two metamorphic ages did not show any structural and chemical difference, although the ca. 1916 Ma zircon grains exhibit slightly smaller in size (sample 11XSZ02 in Fig. 8).

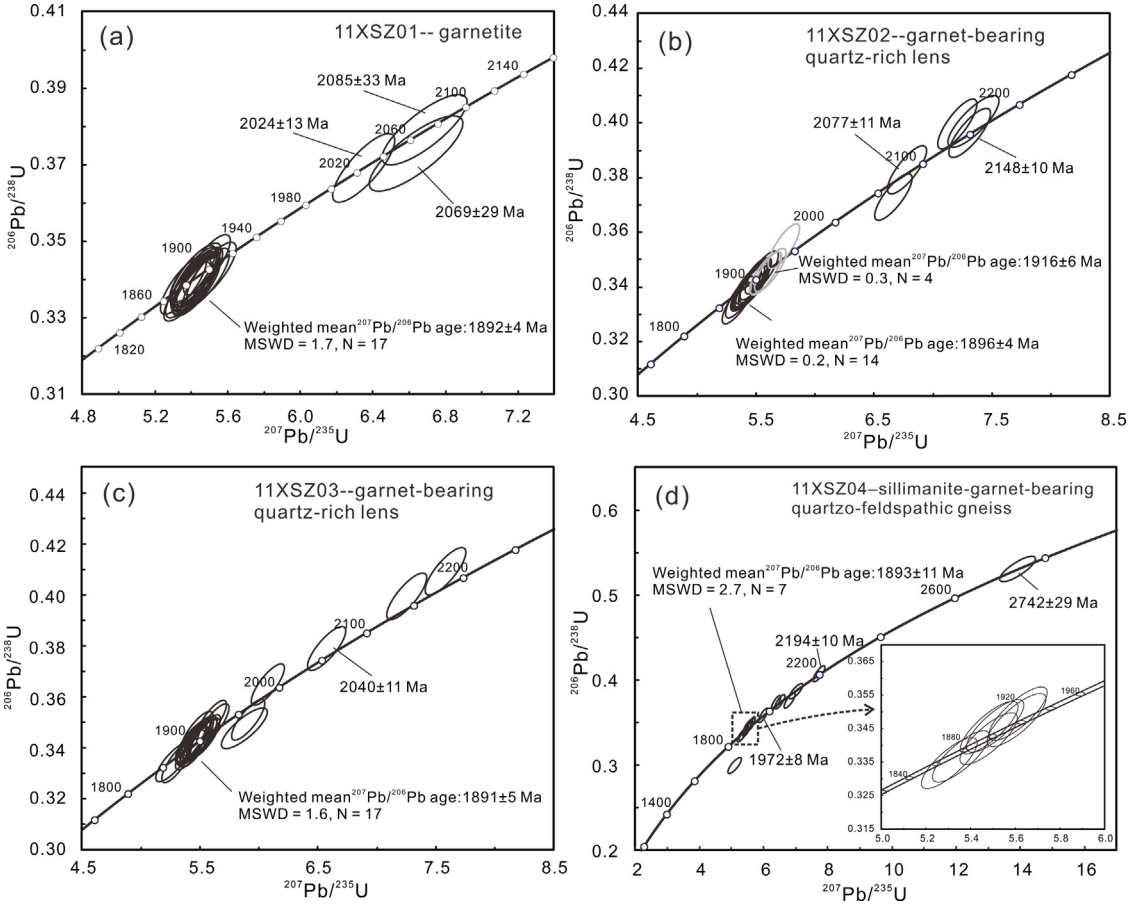

Fig. 9. Concordia diagrams of zircon SIMS U–Pb analytical results from the collected samples 11XSZ01-04. Ellipses represent 1σ error.

Table 1
Age summary of the metamorphic zircons in this study.

Sample	Lithology	Location	Method	Th (ppm)	U (ppm)	Th/U	Metamorphic age (Ma)
11XSZ01	Garnetite	Xiaoshizi	SIMS	37–254	104–1076	0.05–0.69	1892 ± 4
11XSZ02	Grt-bearing Qz-rich lens	Xiaoshizi	SIMS	19–303	353–942	0.05–0.78	1896 ± 4 and 1916 ± 6
11XSZ03	Grt-bearing Qz-rich lens	Xiaoshizi	SIMS	47–353	353–685	0.08–0.65	1891 ± 5
11XSZ04	Sil-Grt-bearing quartzo-feldspathic gneiss	Xiaoshizi	SIMS	181–223	440–587	0.34–0.41	1893 ± 11
11XSZ06	Sil-Grt-bearing quartzo-feldspathic gneiss	Xiaoshizi	LA-ICP-MS	28–155	97–419	0.21–0.37	1881 ± 7 and 1910 ± 7
11XSZ07	Quartz vein	Xiaoshizi	LA-ICP-MS	38–163	332–918	0.07–0.40	1883 ± 4
11XSZ17	Grt-bearing quartzo-feldspathic gneiss	Xiaoshizi	LA-ICP-MS	31–68	107–612	0.11–0.29	1932 ± 8
11XXG04	Grt-bearing quartzo-feldspathic gneiss	Zhuozi	LA-ICP-MS	20–279	401–637	0.04–0.51	1881 ± 5 and 1854 ± 7

Note: Th, U contents and Th/U ratios are those from unzoned zircon overgrowths/grains.

The detrital cores/grains have Th contents of 76–302 ppm, U contents of 203–1195 ppm, and Th/U ratio of 0.16–0.56. Whereas, all unzoned overgrowths/grains show Th ranging from 19 ppm to 303 ppm, U from 353 ppm to 942 ppm, and Th/U ratio of 0.05–0.78.

5.1.3. Sample 11XSZ03

Twenty-six spots were analyzed by SIMS, but two discordant spots were omitted from further calculation (Supplementary Table 1). Six detrital zircon cores/grains yield U–Pb ages in a range from 1967 ± 4 Ma to 2155 ± 5 Ma, slightly below or above concordia (Fig. 9c). The remaining seventeen unzoned overgrowths/grains generate a concordant weighted mean $^{207}Pb/^{206}Pb$ age of 1891 ± 5 Ma (MSWD = 1.6; Fig. 9c).

The detrital cores/grains show Th contents of 36–607 ppm, U contents of 181–1219 ppm, and Th/U ratio of 0.43–0.60. Whereas, the other unzoned overgrowths/grains show Th of 47–353 ppm, U of 353–685 ppm, and Th/U ratio of 0.08–0.65.

5.1.4. Sample 11XSZ04

Sixteen spots were analyzed by SIMS, with one discordant data excluded from further calculation (Supplementary Table 1). The detrital cores/grains show U–Pb ages that scatter mainly from 1972 ± 8 Ma to 2194 ± 10 Ma, even with one concordia age of 2742 ± 29 Ma (Supplementary Table 1; Fig. 9d). Seven analyzed unzoned overgrowths/grains yield a concordant weighted mean $^{207}Pb/^{206}Pb$ age of 1893 ± 11 Ma (MSWD = 2.7; Fig. 9d).

The detrital cores/grains show Th contents of 53–276 ppm, U contents of 241–1065 ppm, and a wide spread of Th/U ratio, from 0.05 to 0.23, and then from 0.48 to 0.71. In contrast, the unzoned overgrowths/grains have Th contents of 181–223 ppm, U contents of 440–587 ppm, and correspondingly a tight Th/U range of 0.34–0.41.

5.1.5. Sample 11XSZ06

Nineteen valid spots are listed in Supplementary Table 2 and plotted in Fig. 10a after deletion of several spots which show large

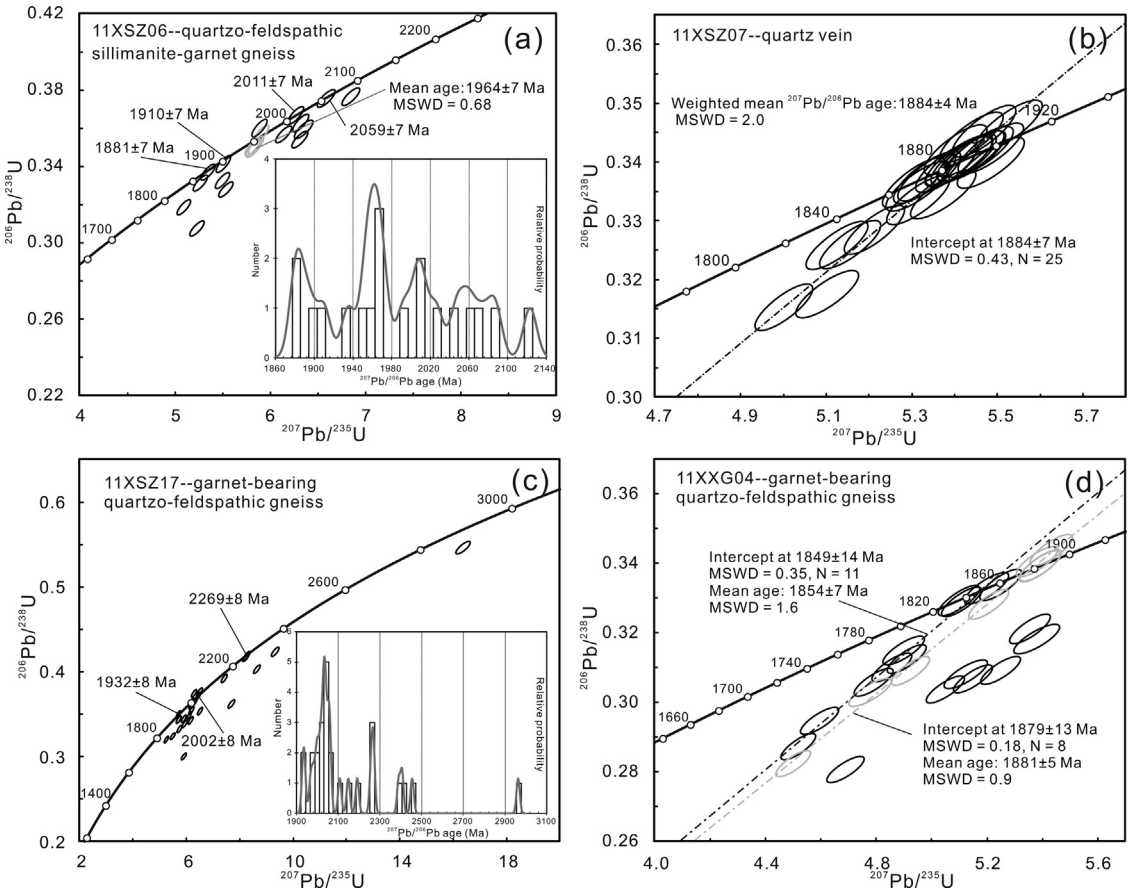

Fig. 10. Concordia diagrams and/or histogram of distribution of $^{207}Pb/^{206}Pb$ ages of zircon LA-ICP-MS U–Pb analytical results from the collected samples 11XSZ06-07, 11XSZ17 and 11XXG04. Ellipses represent 1σ error.

analytical error or inverse discordance. Most analyses were performed on the detrital cores/grains, and only four on metamorphic unzoned overgrowths/grains. The detrital cores/grains yield U–Pb ages mainly scattering from 1964 ± 6 Ma to 2059 ± 6 Ma (Fig. 10a). In addition, two concordia metamorphic ages of 1881 ± 7 and 1910 ± 7 Ma are identified.

The detrital cores/grains show Th ranging from 33 ppm to 1016 ppm, U from 125 ppm to 491 ppm, and Th/U ratio from 0.10 to 2.22. Whereas, the metamorphic overgrowths/grains show Th contents of 28–155 ppm, U contents of 97–419 ppm, and Th/U ratio of 0.21–0.37.

5.1.6. Sample 11XSZ07

Thirty-four spots were analyzed by LA-ICP-MS, but ten spots were excluded from further calculation because of inverse discordance or large analytical error (Supplementary Table 2). All the remaining data were obtained from the unzoned overgrowths/grains, which are plotted on or below the concordia with an upper intercept age of 1884 ± 7 Ma (MSWD = 0.43), consistent with their weighted mean $^{207}Pb/^{206}Pb$ age of 1884 ± 4 Ma (MSWD = 2.0; Fig. 10b). Th and U contents of these unzoned overgrowths/grains are 38–163 ppm and 332–918 ppm, with their Th/U ratio scattering in a range of 0.07–0.40.

5.1.7. Sample 11XSZ17

Twenty-six valid spots are listed in Supplementary Table 2 and plotted in Fig. 10c without the inverse discordant data or those with large analytical error. Most of the analyses were performed on the detrital cores/grains, which yield U–Pb ages scattering mainly from 1968 ± 8 Ma to 2454 ± 8 Ma, even up to 2962 ± 8 Ma, with a peak at ca. 2040 Ma (Fig. 10c). Only one zircon yields concordia metamorphic age 1932 ± 8 Ma. Th, U contents and Th/U ratio of the detrital cores/grains scatter from 20 ppm to 710 ppm, from 49 ppm to 1025 ppm, and from 0.02 to 1.66, respectively. Th and U contents of two zircon overgrowths are 31–68 ppm, 107–612 ppm, with their Th/U ratio of 0.11–0.29.

5.1.8. Sample 11XXG04

Thirty spots were analyzed by LA-ICP-MS, but five spots were omitted because of large analytical error or inverse discordance. U–Pb data from detrital cores/grains are all plotted below the concordia, of which $^{207}Pb/^{206}Pb$ ages range from 1964 ± 8 Ma to 2002 ± 7 Ma. The remaining unzoned overgrowths/grains have defined two major age groups, which upper intercept at 1849 ± 14 Ma (1: MSWD = 0.35; N = 11) and 1879 ± 13 Ma (2: MSWD = 0.18; N = 8) (Fig. 10d), consistent with their individual weighted mean $^{207}Pb/^{206}Pb$ ages of 1854 ± 7 Ma (MSWD = 1.6) and 1881 ± 5 Ma (MSWD = 0.9).

The detrital cores/grains show Th contents of 17–105 ppm, U contents of 633–812 ppm, and a tight range of Th/U ratio from 0.03 to 0.17. In contrast, Th, U contents and Th/U ratio of the younger population of the unzoned overgrowths/grains are spread from 21 ppm to 279 ppm, from 412 ppm to 566 ppm, and from 0.08 to 0.51, respectively, whereas those of the older population are 20–73 ppm, 401–637 ppm, and 0.04–0.15.

5.1.9. Summary

The unzoned zircon overgrowths/grains in the four samples involving the garnetite, garnet-bearing quartz-rich lenses and the adjacent country rock of sillimanite–garnet-bearing quartzo-feldspathic gneiss (samples 11XSZ01-04) generate similar age of ca. 1890 Ma (Fig. 9 and Table 1); whereas, the unzoned zircon

overgrowths/grains in other quartz-feldspathic gneisses and quartz vein (samples 11XSZ06-07, 11XXG04) yield similar age of ca. 1884 Ma (Fig. 10; Table 1). The slight age gap between 1890 Ma and 1884 Ma may be caused by differences between the analytical methods (Table 1). In addition, samples 11XSZ02, 11XSZ06 and 11XSZ17 also yield older metamorphic ages of ca. 1916 Ma, but sample 11XXG04 records a younger metamorphic age of 1854 ± 7 Ma (Table 1). Most of the detrital cores/grains of the samples in this study yield ages mainly scattering from 1964 ± 8 Ma to 2454 ± 8 Ma, suggesting their provenances are mainly supplied by the older than ca. 1960 Ma magmatism in Paleoproterozoic (Figs. 9 and 10).

5.2. Morphology and geochronology of monazite

Monazite chemical dating was undertaken only for the garnetite (samples 09DSZ20 and 09DSZ20′, which are different thin sections from the same hand specimen). Most of crystals are homogenous in structure, but minor variations occur, with brighter small core and/or thin rims (Fig. 11b, d), or irregular bright patches present related to variance in Y and Th contents (Fig. 11b). A total of 115 spots were measured, with 7 excluded from age calculation because of very low Th contents and associated large errors. A broad spread of apparent ages was obtained from 1777 ± 32 Ma to 1919 ± 30 Ma (Supplementary Table 3). These apparent ages did not exhibit significant correlations with internal zoning in the monazites, with the exception that BSE-bright patchy areas usually yielded younger ages, such as 1777 ± 32 Ma in Fig. 11b. The older ages were generally obtained from those monazites occurring as inclusions in garnet (Fig. 11a–f), although it should be noted that some inclusion grains yielded younger ages (Fig. 11g–j). Matrix monazites generally yielded younger ages, whether the grains were adjacent to sillimanite or ilmenite (Fig. 11k and l).

Population-based analysis of the monazite chemical age data reveals four major age peaks or groups on a $^{207}Pb/^{206}Pb$ age histogram (Fig. 12). i. 1915 ± 30 Ma (MSWD = 0.006) obtained from

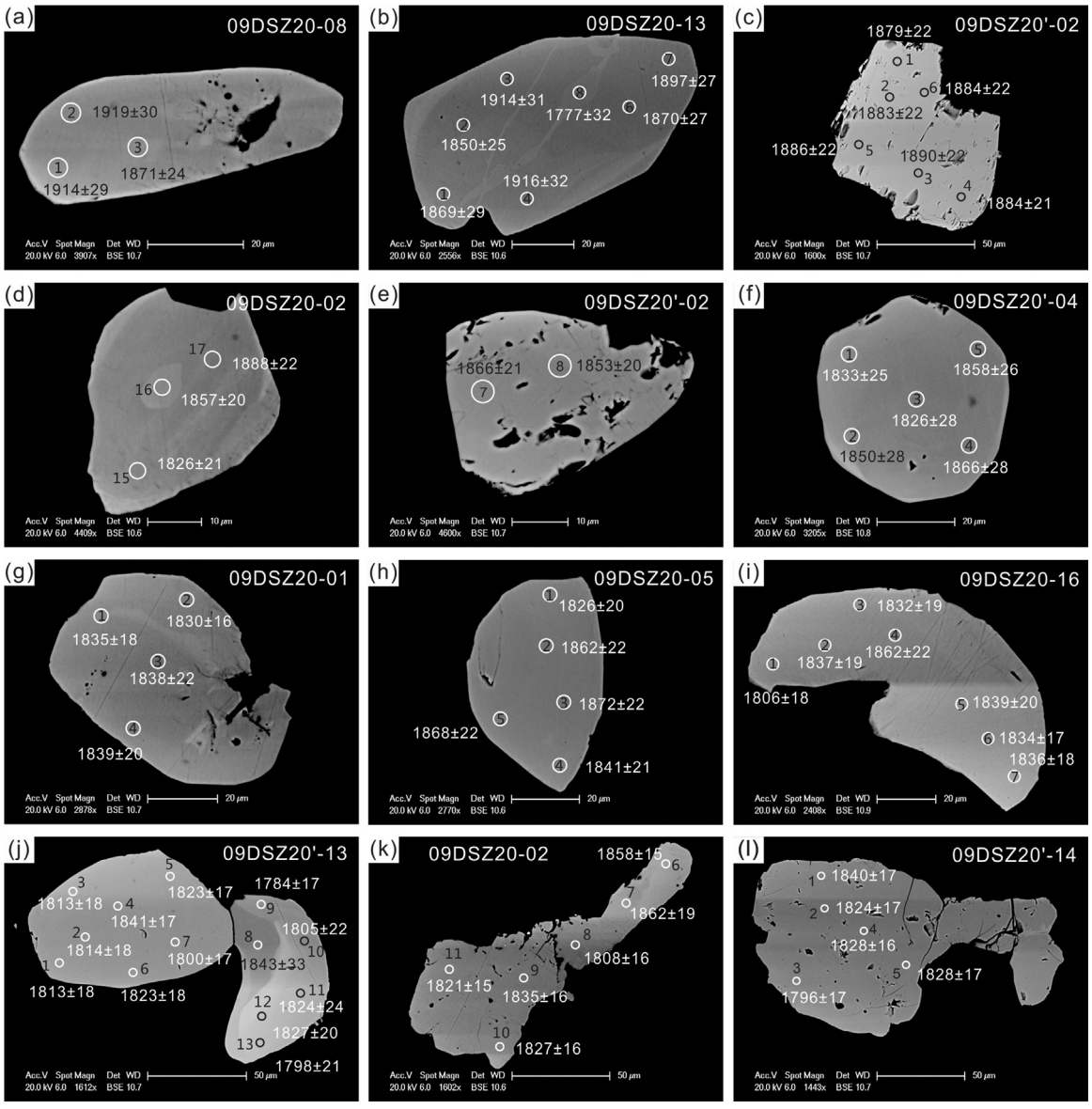

Fig. 11. Back-scattered electron (BSE) imaging of the monazite grains from the garnetite showing the apparent U–Th–Pb ages and analyzed numbers. (a) Monazite in mantle of garnet and coexisting with rutile and zircon; (b) monazite in mantle of garnet lonely; (c) monazite in core of garnet and coexisting with rutile, zircon and plagioclase; (d) monazite in mantle of garnet and coexisting with rutile; (e) monazite in core of garnet and coexisting with rutile, zircon and plagioclase; (f and g) monazite in mantle of garnet lonely; (h) monazite in mantle of garnet and coexisting with quartz; (i) monazite in core of garnet and coexisting with apatite; (j) monazite in mantle of garnet associated with plagioclase; (k) monazite between garnet and sillimanite in matrix; and (l) monazite between garnet and sillimanite in matrix, associated with ilmenite.

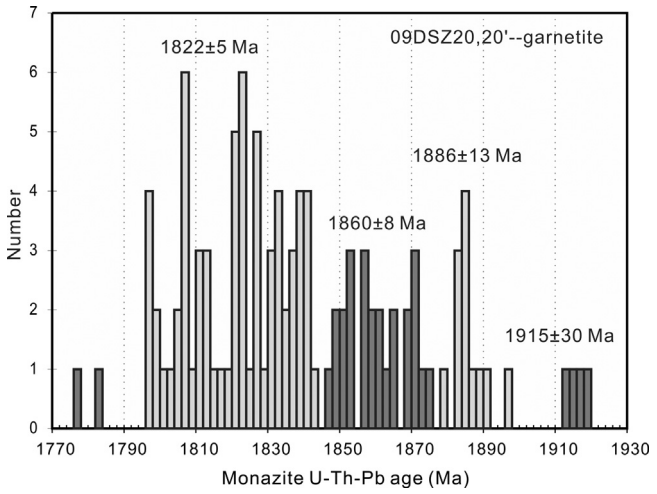

Fig. 12. Histogram for the distribution of monazite U–Th–Pb ages of the garnetite.

four spots; ii. 1886 ± 13 Ma (MSWD = 0.034) obtained from 12 spots; iii. 1860 ± 8 Ma (MSWD = 0.15) from 25 spots; iv. 1822 ± 5 Ma (MSWD = 0.48) from 65 spots. The remaining two spots, from the disturbed bright-BSE branches (Fig. 11b), yield the youngest ages, 1777 ± 32 Ma and 1784 ± 17 Ma. The oldest monazite chemical age peak is comparable with the zircon U–Pb age of 1916 ± 6 Ma obtained by sample 11XSZ02, and the second monazite age peak is indistinguishable from ages of ca. 1890 Ma obtained from the unzoned zircon overgrowths/grains from samples 11XSZ01-04, 11XSZ06-07 and 11XXG04. The third monazite age peak overlaps with the group age of 1854 ± 7 Ma obtained from zircon overgrowths/grains in sample 11XXG04. The fourth monazite age peak is distinct younger than all of the zircon U–Pb ages obtained in this study.

6. Trace element (and major element for garnet) compositions

6.1. Zircon

Four samples (11XSZ01-02, 11XSZ07, and 11XXG04) were chosen for trace elements analyses, which are listed in Supplementary Table 4 and plotted in Fig. 13. Rutile and quartz are present in all samples, and so allow direct application of the Ti-in-zircon thermometer (Watson et al., 2006) to these assemblages.

Trace element analyses of zircons in sample 11XSZ01 were mainly obtained from the unzoned overgrowths/grains that yielded ages of ca. 1890 Ma, both from separated grains in mount and those located in situ where textural setting can be correlated. The overgrowths/grains exhibit pronounced negative Eu anomalies (Eu/Eu* = 0.02–0.17), positive Ce anomaly (Ce/Ce* = 0.97–75.67), and strong enrichment in HREE with value of 50–1000 times chondrite (Fig. 13a). The REE pattern is characterized by steeply positive LREE profiles from La to Sm, and steeply positive to nearly flat HREE profiles from Gd to Lu (Lu_N/Gd_N = 40.36–1.10). Zircon overgrowths/grains located in the mantle of garnet porphyroblasts contain higher HREE (from Gd to Lu) with about 1000 times chondrite compared with those in contact with garnet rims and those in the matrix, which contain HREE at about 100 times chondrite. Zircon enclosed by sillimanite shows similar characteristics with those between garnet and sillimanite in the matrix. The Eu anomaly is more pronounced in grains containing lower HREE. Y contents scatter over range of 109–1098 ppm, and are positively correlated with HREE contents. Ti contents range from 18 ppm to 31 ppm, and the corresponding temperatures calculated from the Ti-in-zircon thermometer are 796–851 °C, with an average value of 820 °C.

Zircon trace element analyses of sample 11XSZ02 were obtained from unzoned zircon overgrowths/grains, which show similar characteristics to those in sample 11XSZ01: enrichment in HREE at about 100–1000 times chondrite compared to LREE and a negative Eu anomaly (Eu/Eu* = 0.03–0.50, Fig. 13b). Their positive Ce anomaly is not obvious, and even negative Ce is obtained. The LREE pattern is positive from La to Lu and the HREE pattern steeply positive or nearly flat from Gd to Lu (Lu_N/Gd_N = 32.86–1.03). Eu anomaly (Eu/Eu* = 0.50 vs. 0.03) is more pronounced in grains containing less HREE. Y contents scatter from 119 ppm to 968 ppm and are positively correlated with HREE. Ti contents of analyzed grains scatter from 19 ppm to 35 ppm, and the corresponding temperatures calculated from the Ti-in-zircon thermometer are 800–864 °C, with an average value of 828 °C.

Two detrital cores/grains and twenty-four unzoned overgrowths/grains were analyzed to document the zircon trace element characteristics in sample 11XSZ07. The detrital zircon cores/grains show slightly higher REE contents, no Ce anomaly (Ce/Ce* = 0.88–1.35 vs. 4.56–11.7), and a less pronounced negative Eu anomaly (Eu/Eu* = 0.43–0.55 vs. 0.01–0.03) than the unzoned overgrowths/grains (Fig. 13c). Both populations of the zircon grains reveal steeply positively sloping LREE patterns from La to Sm, and slightly negatively sloping HREE patterns from Gd to Lu (Lu_N/Gd_N = 0.32–0.44; Fig. 13c) at about 20–100 times chondrite. Y contents of two detrital grains are 120 ppm and 143 ppm. In contrast, most of the unzoned overgrowths/grains contain lower Y (56–130 ppm), positively correlated with HREE. Ti contents of the two types of zircon grains overlap from 15 ppm to 36 ppm, and their calculated Ti-in-zircon temperatures are 776–867 °C, with an average value of 841 °C.

Seven detrital cores/grains and fifteen unzoned overgrowths/grains were analyzed in sample 11XXG04. The detrital cores/grains contain slightly higher REE contents than the unzoned overgrowths/grains, although they both preserve positive Ce anomalies (Ce/Ce* = 1.37–8.21 vs. 1.25–10.9), negative Eu anomalies (Eu/Eu* = 0.02–0.17 vs. 0.02–0.31), positive LREE slopes from La to Sm and nearly flat HREE patterns from Gd to Lu (Lu_N/Gd_N = 1.57–3.14 vs. 0.53–4.33) at 50–300 times chondrite (Fig. 13d). Unzoned overgrowths/grains contain less Y (86–275 ppm) than the detrital cores/grains (105–436 ppm), although there is some overlap. Y contents are positively correlated with HREE content. Ti in the two types of grains overlap, with unzoned overgrowths/grains containing slightly higher values (Ti = 18–29 vs. 20–40 ppm). The calculated Ti-in-zircon temperatures of the two types of zircons are 795–843 °C (avg. 823 °C) and 806–879 °C (avg. 830 °C), respectively.

6.2. Monazite

REEs of the analyzed monazite grains are strongly rich in LREE with 3–4 × 10^5 times chondrite compared to HREE, and reveal variable negative Eu anomaly (Eu/Eu* = 0.01–0.07; Fig. 14a). Monazites as inclusions in garnet reveal a slightly negative LREE slope from La to Sm, whereas the grains in the matrix a slightly positive LREE slope. HREE contents and patterns of these monazite grains are indistinguishable, with the inclusion-type grains overlapping the matrix grains. Y contents of the monazite grains scatter in a range of 730–13,323 ppm and show a positive correlation with HREE (Supplementary Table 5). The La_N/Sm_N–Y diagram allows a detailed comparison of the different populations of monazite grains (Fig. 14b). Those grains yielding the youngest ages reveal the lowest Y contents and La_N/Sm_N ratios, although a wide scatter is present. Four grains with the oldest ages show higher Y contents and the highest La_N/Sm_N ratios. Those grains yielding ages of ca. 1860 and

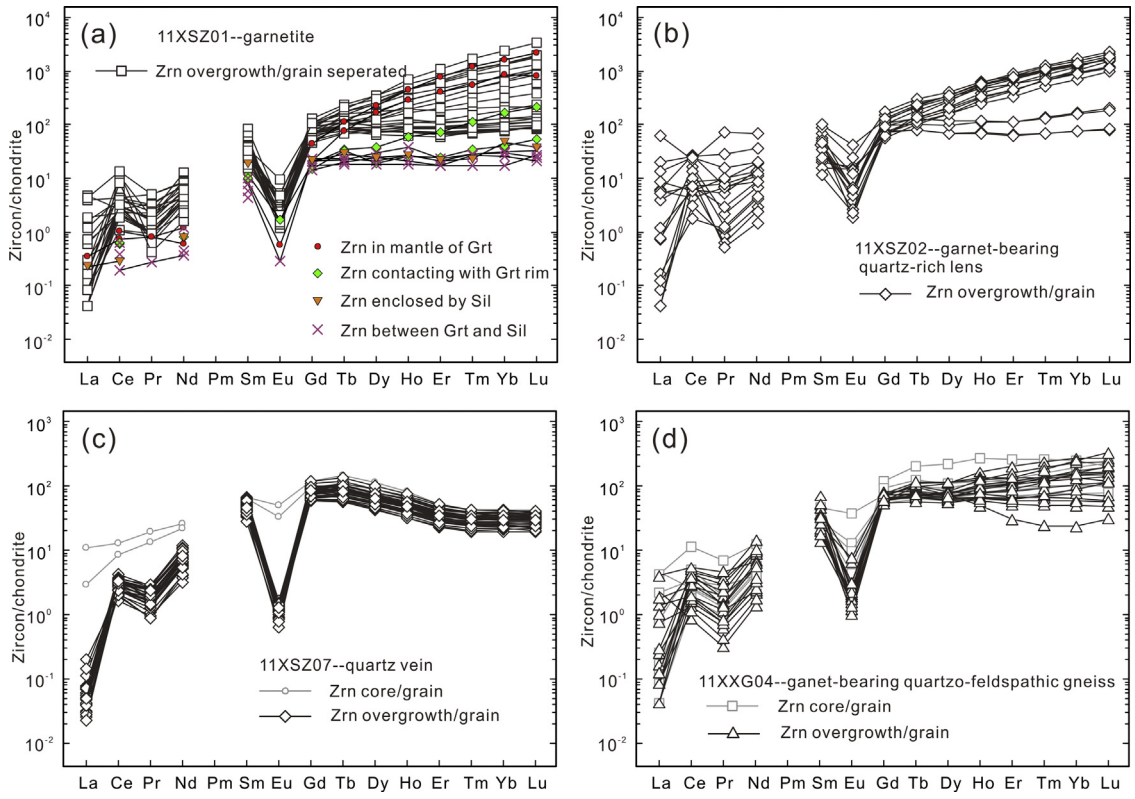

Fig. 13. Chondrite-normalized REE patterns for the zircon grains from samples 11XSZ01-02, 11XSZ07 and 11XXG04. Chondrite normalization is according to Sun and McDonough (1989). In sample 11XSZ01, both zircon grains separated from the rock and those in thin sections are analyzed for comparison.

ca. 1886 Ma show similar characteristics: the highest Y contents are associated with higher La_N/Sm_N ratios. Th, U, Pb contents of monazite grains vary over the ranges 5650–116,815 ppm, 1439–25,701 ppm, and 3541–13,988 ppm, respectively, and their corresponding Th/U ratios scatter from 1 to 72.

6.3. Garnet

Major and trace element analyses of garnet grains were conducted in the garnetite and associated garnet-bearing quartz-rich lens. Five types of garnet grains are distinguished based on their different grain sizes and microstructural positions (Supplementary Tables 6 and 7; Figs. 15 and 16). Garnet poikiloblasts (>4 mm) with abundant quartz inclusions, in the matrix mainly composed of quartz are labeled as garnet A (Fig. 4e). Garnet poikiloblasts (2.5–4 mm) with rare sillimanite and biotite inclusions in mantle, but without abundant quartz inclusions, in the matrix composed of mainly quartz and plagioclase are labeled as garnet B (Fig. 4a). Garnet poikiloblasts similar to garnet B, but in a matrix made up of sillimanite with no quartz are labeled as garnet C (Fig. 4b). The coronal garnet (<0.2 mm) associated with cordierite around large garnet poikiloblasts or on sillimanite is labeled as garnet D; the five spots are from individual grains as they are too small for the beam spot of LA-ICP-MS to show any intragranular variation (Fig. 4c). Garnet grains (ca. 2.5 mm) with rare inclusions from the garnet-bearing quartz-rich lens are labeled as garnet E (Fig. 4f).

All garnet types are pyrope (25–38%)-almandine (58–70%) solid solutions with minor grossular (2.5–4.5%) and spessartine (0.5–1.0%). All display a large or small plateau area of constant X_{Mg} and a diffusional rim, in which X_{Mg} decreases from 0.39–0.40 to 0.35–0.32 (Fig. 15a). Cores of garnet E show slightly higher X_{Mg} (ca. 0.41) than the other garnets (ca. 0.38); garnet D has the lowest X_{Mg} (0.30–0.32; Fig. 15a). Garnet types A, B (large) and E show distinctly continuous decreases in grossular from cores toward rims (bell-shaped, from 3.5% to 2.7%), whereas garnet C shows only a slight decrease from 3.3% to 2.7%, and garnet B (small) has almost constant grossular (ca. 3.0%; Fig. 15b). Garnet D contains the highest grossular (3.7–4.1%) among the analyzed garnet grains (Fig. 15b).

HREE (from Gd to Lu) and Y contents display pronounced bell-shaped zoning in garnets A, B (large), but exhibit only moderate zoning or are constant in the other garnet types (Fig. 15c–e). Y contents vary between 117 ppm and 689 ppm, with cores of garnet A showing the highest values (Fig. 15c). Yb and Dy scatter in the range 7–147 ppm, 22–98 ppm, respectively, with garnet A cores again preserving the highest values (Fig. 15d–e). Sm (MREE) contents increase slowly from cores to rims in garnet A, but decrease rapidly in the outmost part of the rim, whereas these elements decrease slightly from cores to rims in the other garnet grain types (Fig. 15f). Garnet E contains the highest Sm contents (13–18 ppm), and garnet D the lowest (2–3 ppm) with the other in a range of 5–15 ppm (Fig. 15f). Ti contents in garnet A increase from cores to rims and then decrease suddenly in the outmost part of the rims. In contrast, Ti contents in garnet B (large) decrease from cores to mantles and then increase in the rims, with the inner part of the rims showing the highest contents as Ti decreases again toward the outermost part of the rims (Fig. 15g). Ti contents decrease slightly from cores to rims in garnet B (small) and garnet C (Fig. 15g), whereas they increase rimwards in garnet E (Fig. 15g). Among these grains, garnet E shows the highest Ti contents of 343–569 ppm, with the other grain types scattering from 7 ppm to 234 ppm (Fig. 15g). Cr contents in garnets A and B exhibit slightly inverse bell-shaped zoning, whereas Cr is constant in the other grains. Garnet E contains the highest Cr contents of 354–451 ppm, garnet D contains high Cr contents of 347–378 ppm, and garnet C the lowest contents at 136–167 ppm (Fig. 15h). V contents decrease continuously from cores to rims in garnet B (small), and stay constant in core–mantle of garnet C, and decrease in the rim, whereas almost stay constant in the other grains (Fig. 15i). Garnet E contains the highest V

contents of 145–202 ppm with the other scattering over the range of 70–151 ppm (Fig. 15i). Li contents increase from cores to rims in garnets B (small) and C, but are constant in the other grains (Fig. 15j). Garnet D shows the highest Li contents (11–15 ppm) compared to the other garnet types (4–10 ppm) (Fig. 15j). Zn contents of all garnet grains display the bell-shaped zoning (except garnet D), but generally are constant in the core–mantle region of garnet C, and vary from 49 ppm to 307 ppm in all the analyzed grains (Fig. 15k). Zr contents decrease slightly from cores to rims in garnets A, B (small), C, but are constant in garnet B (large) (Fig. 15l). In contrast, Zr contents increase continuously from cores to rims in garnet E (from 31 ppm to 114 ppm; Fig. 15l). Garnet D shows the lowest Zr contents of 2–5 ppm, with the other garnet types scattering over the range of 11–114 ppm.

All the analyzed garnet grains show pronounced (Eu/Eu* < 0.05, garnets A–C, E) or slightly negative (Eu/Eu* = 0.10–0.39, garnet D) Eu anomalies, enrichments in HREE at about 100–1000 times chondrite, and flat to positive (Lu_N/Gd_N = 1–15, garnets A–B, C–D) or slightly negative (Lu_N/Gd_N = 0.3–1.0, garnet C) HREE slopes pattern (Fig. 16). Garnet cores usually contain higher HREE than rims, with the large garnet poikiloblast cores such as garnets A and B exhibiting the highest HREE contents. However, although large in size, garnet C exhibits a flat and even negative HREE slope at less than 100 times chondrite, which might reflect its quartz-absent textural setting.

7. Discussion

7.1. Garnet growth during the high-grade metamorphism

Garnet poikiloblasts (at stage M1) in the garnetite exhibit well-preserved bell-shaped grossular zoning which is the result of garnet growth with some diffusional modification at high temperature (Jiao et al., 2013). Zoning in trace elements might better reflect garnet growth, as diffusion coefficients for the trivalent cations are smaller than those for the major divalent cations in the same garnet (Van Orman et al., 2002; Tirone et al., 2005; Carlson, 2012). As compatible elements for garnet, HREE and Y exhibit progressive decreases from cores toward rims in the garnet poikiloblasts, caused by the Rayleigh fractionation of these components during garnet growth and an increase in the volume of melt that will dilute these components (Hollister, 1966; Spear and Kohn, 1996; Bea et al., 1997; Otamendi et al., 2002; Whitehouse and Platt, 2003). However, later diffusion has smoothed or modified these growth zones, such as those developed in the small poikiloblasts (garnets B (small) and C). Garnet C shows a similar grain size to garnet B (large), but contains lower HREE contents, which is related to its textural setting in which sillimanite is abundant, but no partial melt remains. It is well-documented that minerals in leucosomes or metapelite that has undergone significant melting are usually marginally richer in HREE than those in the corresponding restite or metapsammite in which melting was minimal (Rubatto et al., 2001, 2006).

Coronal garnet (garnet D) exhibits higher Gro, Cr and Li contents, but lower X_{Mg}, Sm, HREE, Zn and Zr contents and weaker Eu negative anomalies compared to garnet poikiloblasts (garnets A–C; Fig. 15). These compositional differences reflect a different formation environment and indicate that coronal garnet represents a new growth period rather than a continuation of garnet poikiloblasts growth. High Gro contents and weak Eu negative anomalies suggest that plagioclase does not coexist with coronal garnet, consistent with the petrographical observations. High Cr and Li are interpreted to reflect the breakdown of biotite, which is strongly compatible in these components (Bea et al., 1994). This is supported by the microdomainal reaction analysis that indicates Grt1 (M1) + Sil + Qz + Bt = Grt2 + Crd + Ilm + Liq (Jiao et al., 2013). Low Zn

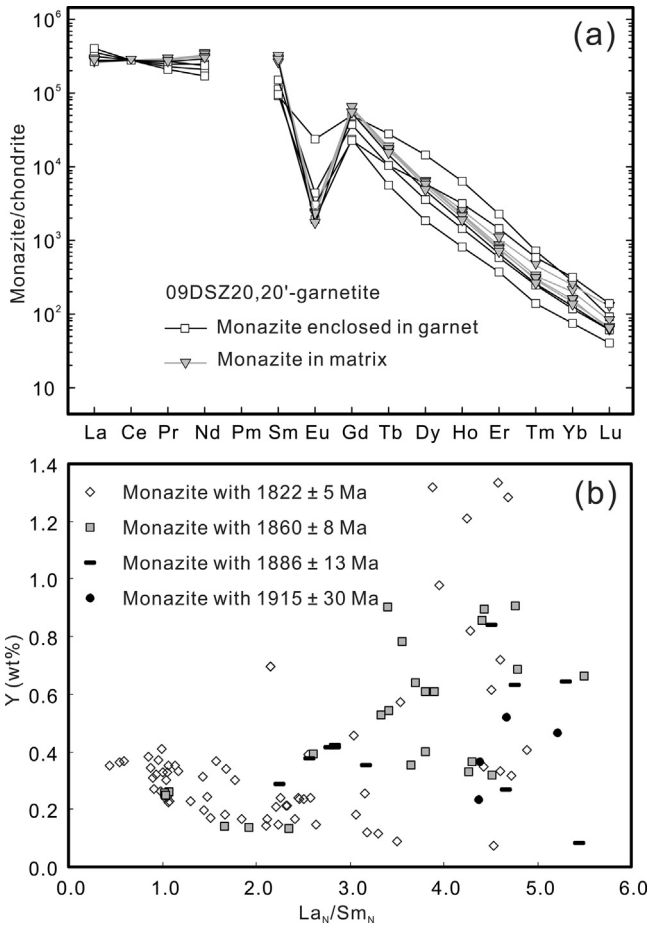

Fig. 14. (a) Chondrite-normalized REE patterns for the monazite grains from sample 09DSZ20, 20′ (garnetite) analyzed by LA-ICP-MS. Chondrite normalization is according to Sun and McDonough (1989). (b) La_N/Sm_N–Y diagram of the four age peaks of monazite grains analyzed by EMP.

contents in the coronal garnet might be related to the formation of coeval Zn-rich spinel. Low Zr contents of the coronal garnet suggest that crystallization of zircon occurred prior to M2 stage, a detail to be discussed further in the following section. Lower HREE contents of the coronal garnet are consistent with the Rayleigh fractionation model for garnet growth, which leads to lower HREE in the surrounding environment after garnet poikiloblast formation. Lower Sm contents of the coronal garnet compared to garnet poikiloblasts might be caused by formation of matrix monazite, which has Sm contents higher than those of the inclusion-type monazite (Fig. 14a).

In garnet-bearing quartz-rich lens, garnet E is rich in Cr, V and Ti reflecting scarcity of coexisting ilmenite that is strongly compatible in these elements, and consistent with the petrographical observations. Lower in HREE compared to garnets A–B suggests that this garnet formed after crystallization of garnets A–B, but diffusion must have modified its HREE zoning. As an incompatible element, Zr partitions preferentially into melt until zircon begins to crystallize, and the inverse bell-shaped pattern of Zr preserved in garnet E suggest that it crystallized directly from the remaining fractionating melt, rather than as a peritectic product as deduced for the garnet poikiloblast in the garnetite.

7.2. Correlation of zircon and monazite to garnet growth

There are several potential mechanisms to explain zircon formation based on previous research (Harley et al., 2007), such as

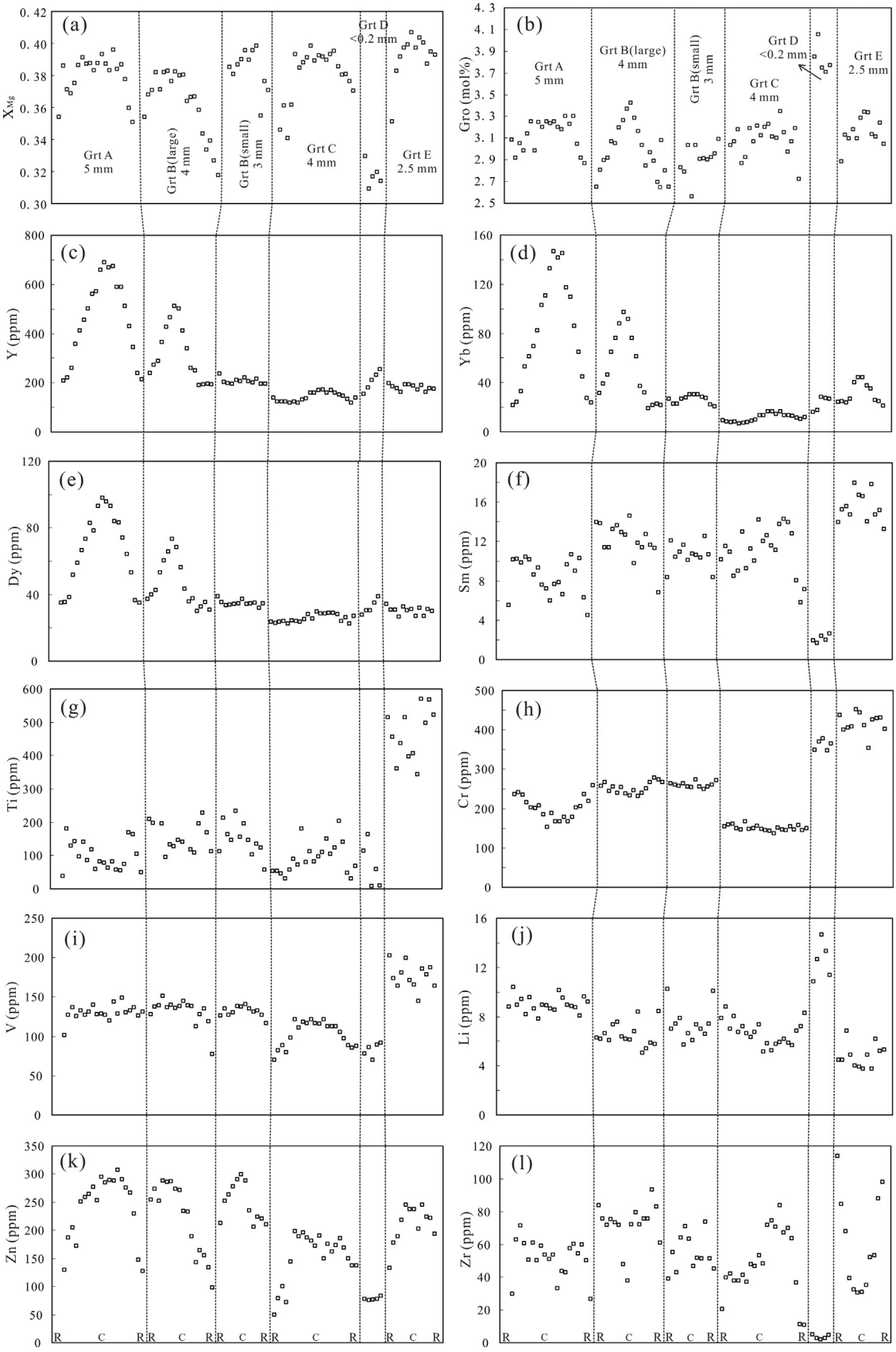

Fig. 15. Variance of chemical compositions of different kinds of garnet grains in terms of X_{Mg} (a), Gro (b), Y (c), Yb (d), Dy (e), Sm (f), Ti (g), Cr (h), V (i), Li (j), Zn (k) and Zr (l) in both the garnetite and garnet-bearing quartz-rich lens. R and C represent rim and core of the garnet, respectively. Refer to the text (6.3 Garnet) for the classification of different garnets.

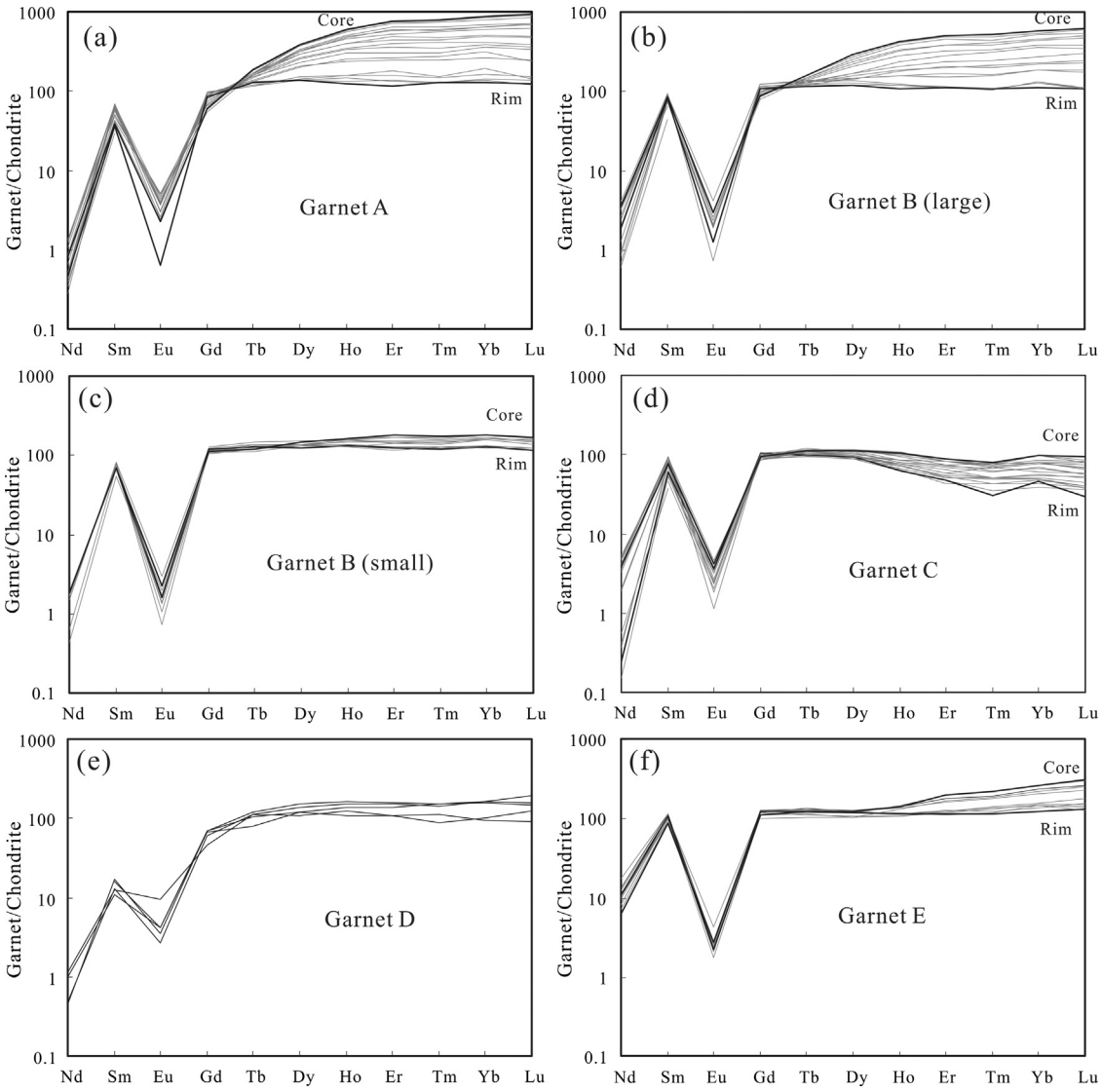

Fig. 16. Chondrite-normalized REE patterns for different kinds of garnet grains. Chondrite normalization is according to Sun and McDonough (1989). Refer to the text (6.3 Garnet) for the classification of different garnets.

(i) net-transfer or exchange reaction of Zr-bearing minerals (Fraser et al., 1997; Bingen et al., 2001; Degeling et al., 2001); (ii) formation from partial melt or during melt crystallization (Roberts and Finger, 1997; Rubatto, 2002; Hermann and Rubatto, 2003; Whitehouse and Platt, 2003); (iii) Ostwald ripening-effect of surface energy minimization that caused the small zircon grains to be dissolved in the contacting melt droplets and coeval re-precipitation on the sites of large zircon grains as overgrowths (Vavra et al., 1999; Nemchin et al., 2001; Ayers et al., 2003); and (iv) recrystallization of the existing zircon during the solid-state metamorphism (Schaltegger et al., 1999; Vavra et al., 1999; Hoskin and Black, 2000; Möller et al., 2002; Bingen et al., 2004).

The irregular zircon grain in contact with ilmenite in the matrix, and those associated with rutile as inclusions in garnet (Fig. 5c and j) are regarded as the result of the net-transfer or exchange reaction of ilmenite/rutile during the retrograde stage of metamorphism (Fraser et al., 1997; Bingen et al., 2001; Degeling et al., 2001). This is confirmed by the lower Zr contents measured in rutile grains associated with zircon compared with those removed from any zircon (Jiao et al., 2013). In contrast, most of the isometric (rounded or elliptical) zircon grains in the garnetites that have ages of ca. 1890 Ma are considered to result from Ostwald ripening during partial melting, and so are synchronous with the formation of peritectic garnet poikiloblasts. Trace elements in both zircon and garnet in this case are buffered by the coexisting melt composition. The key lines of evidence for this interpretation are detailed below.

Firstly, petrographic observations reveal that the isometric zircon grains (ca. 1890 Ma) are generally located in or surrounding the rim/mantle areas of the garnet poikiloblasts, suggesting their coeval crystallization, subsequent to garnet cores. Secondly, inclusions enclosed by zircon are similar to those in the garnet poikiloblasts, involving sillimanite, plagioclase, quartz, biotite, rutile and apatite, and notably the coexistence of gahnite and quartz as inclusions in zircon has also been observed in garnet poikiloblasts. Thirdly, the unzoned zircon grains and overgrowths revealed by the CL imaging are consistent with formation at high-temperature (HT) granulite-facies conditions in which partial melts are likely to be present (Vavra et al., 1999). Fourthly, zircon present as inclusions in the mantle of the garnet poikiloblasts exhibits higher HREE and Y contents than that in the garnet rim, and the matrix-type zircons show the lowest HREE and Y contents. This relationship is consistent with the bell-shaped profile of HREE and Y contents recorded by the garnet poikiloblasts and ascribed above to Rayleigh fractionation during garnet growth and re-growth. Both zircon and garnet

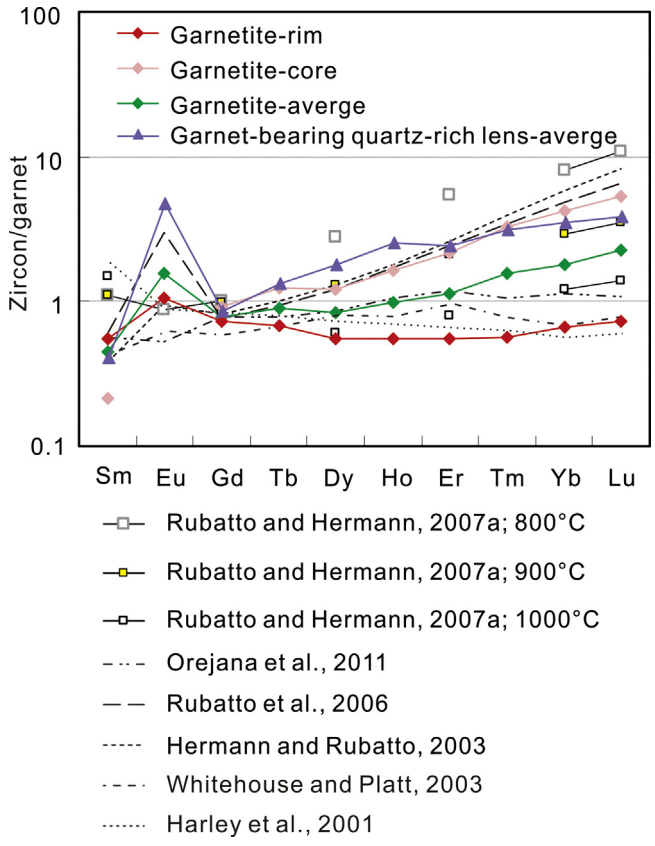

Fig. 17. Calculated partition coefficients between zircon and garnet for MREE-HREE. Garnetite-rim means that zircon with the lowest REE contents verses the garnet rim (Garnet B (large)) in the garnetite. Garnetite-core means that zircon with the highest REE contents verses the garnet core (Garnet B (large)) in the garnetite. Garnetite-average and garnet-bearing quartz-rich lens-average mean the average values of both zircon and garnet in the garnetite and garnet-bearing quartz-rich lens, respectively. The distribution coefficients determined by Harley et al. (2001), Whitehouse and Platt (2003) and Hermann and Rubatto (2003) from metapelitic granulites, Rubatto et al. (2006) from low-pressure metapelitic diatexite (sample SGL5), and Orejana et al. (2011) from granulite xenolith (sample: U145) in granulite-facies metamorphism, and the experimental results at 800 °C, 900 °C and 1000 °C determined by Rubatto and Hermann (2007a), are plotted for comparison.

exhibit variable HREE and Y contents during growth, suggesting that they grew contemporaneously.

HREE partition coefficients (D_{HREE}(zrc/grt)) between zircons and representative garnet poikiloblasts (garnet B (large) without inclusion-rich core) are plotted in Fig. 17. Regardless of which coupling is used, average zircon/average garnet composition (garnetite-average), the highest HREE contents in both zircon and garnet (garnetite-core), or the lowest HREE contents in both zircon and garnet (garnetite-rim), similar partitioning patterns are obtained that are consistent with the previously published D_{HREE}(zrc/grt) data for different *P–T* conditions and garnet major element compositions. These D_{HREE}(zrc/grt) patterns reflect equilibrium between zircon and garnet poikiloblasts during their growths. Rubatto and Hermann (2007a) reported experimentally that the slightly positive profile for D_{HREE}(zrc/grt) from Gd to Lu occurs at lower temperature than the flat D_{HREE}(zrc/grt) profile (800 °C vs. 1000 °C). Based on their experiments, the garnetite-cores with higher D_{HREE}(zrc/grt) would reflect lower temperatures than the garnetite-rim, implying heating during garnet growth. This is consistent with the prograde partial melting process. In contrast to the systematics displayed by the garnetite, the D_{HREE}(zrc/grt) calculated for the garnet-bearing quartz-rich lens shows slightly higher Eu, Tb, Dy and Ho, but lower Yb and Lu compared with the garnetite-core. This reflects disequilibrium between zircon and the garnet in this case and is in agreement with the above conclusion that garnet E crystallized from the fractionating melt, whereas zircon is produced earlier in the partial melting process.

In support of the interpretation presented above, Ti-in-zircon temperatures yielded by zircon grains in the garnetite are ca. 820 °C, consistent with the temperature conditions obtained from stage M1. Moreover, if zircon has crystallized later than garnet poikiloblasts during cooling and crystallization of the remaining melt, its HREE pattern would have been a flat pattern with about 100 times chondrite like that of garnet poikiloblast rims, which is not observed in this case.

Based on all of the lines of evidence, it is concluded that the isometric zircon grains with ages of ca. 1890 Ma crystallized coevally with mantle/rim of the garnet poikiloblasts during partial melting. Zr was supplied by Ostwald ripening in the presence of small melt fractions through dissolution of smaller zircon grains and simultaneous re-precipitation on the larger grains as overgrowths from locally supersatured melt/fluid (e.g. as described and modeled by Watson, 1996). The potential source mineral biotite undergoing incongruent melting, could not itself supply sufficient Zr for zircon formation, and the total zircon overgrowth volume corresponds to a mass far larger than the zircon saturation limit of the coexisting melt during the partial melting (Vavra et al., 1999; Nemchin et al., 2001; Ayers et al., 2003; Kawakami et al., 2013). During the high temperature partial melting episode, inherited zircon or many tiny zircon grains/overgrowths (<5 μm) might be dissolved or lost, and new melt-related zircon precipitated (Rubatto and Hermann, 2007b; Harley et al., 2007). No subsolidus recrystallization sector zoning features are recognized in these zircon grains.

It has been demonstrated that the monazite is less resistant than zircon during slow cooling in high heat flow regimes, and could therefore record variable age information (Högdahl et al., 2012). This is the case here in which at least four monazite population age peaks have been distinguished. Inclusion-type monazites preserved within garnet poikiloblasts usually record older ages such as ca. 1915 Ma and ca. 1886 Ma, and might have formed coevally with the garnet poikiloblast as well as with most zircon grains (ca. 1915 Ma or 1890 Ma) during stage M1. The matrix monazite grains in contact with ilmenite or sillimanite that have higher Sm contents might coexist with coronal garnets that contain lower Sm contents. However, younger and variable ages yielded by all the monazite grains such as from ca. 1860 Ma to ca. 1820 Ma suggest the strong thermal event might have modified their U–Th–Pb systems after initial monazite formation.

7.3. Interpretation of zircon and monazite U–Th–Pb ages

Based on the discussion above, the major age group of ca. 1890 Ma yielded by zircon U–Pb dating and monazite chemical dating is representative of the timing of M1 stage in the garnetite. At this stage the peritectic garnets had already formed in the residuum, free of effects from the regional syn-collisional metamorphism and deformation, in association with coexisting minerals such as sillimanite, quartz, plagioclase and biotite. Granitic melts migrated away from their sources, subsequently segregating and crystallizing elsewhere to produce at least some of the S-type granitoids present in the Khondalite Belt (e.g. Liangcheng area). After melt separation (mainly the K, Na-rich part), the residual melt that did not escape crystallized later as quartz, plagioclase, and melt pseudomorphs between the garnet grains, and produced retrograde biotite around garnet by garnet-melt back reaction. The *P–T* path involving the near-isothermal decompression and subsequent cooling and decompression recorded by the garnetite is representative of the extension/exhumation stage after the continental collision between the Yinshan and Ordos Blocks along the Khondalite Belt (Jiao et al., 2013). Consequently, the age of ca.

Table 2
Representative Palaeoproterozoic geochronological data from the Khondalite Belt, North China Craton.

Rock	Location	Ages (Ma)	Method	Interpretation	Reference
~1.95 Ga					
Grt-Sil-Crd gneiss	Qianlishan terrane	1949 ± 12	LA-ICP-MS	Metamorphic age	Yin et al. (2009)
Grt-Sil-Bt gneiss		1941 ± 24			
Grt-bearing feldspathic quartzite	Helanshan terrane	1958 ± 7	LA-ICP-MS	Metamorphic age	Yin et al. (2011)
Grt-Bt gneiss		1953 ± 7			
Grt-Sil-Bt gneiss		1952 ± 9			
Grt-Sil-Crd gneiss		1955 ± 15			
Grt-Crd gneissic migmatite		1946 ± 13			
Grt-Sil-Crd gneiss		1963 ± 15			
Grt-Crd gneiss		1962 ± 14			
Crustal carbonatite	Daqingshan terrane	1951 ± 5	SIMS-SHRIMP	Formation age of the carbonatite	Wan et al. (2008)
Diopsidite enclave (zircon core)		1954 ± 27		Age of high-grade metamorphism	
Diopsidite enclave (zircon rim)		1944 ± 40		Age of crustal carbonatite magamatism	
Grt-Bt gneiss	Daqingshan terrane	1953 ± 13	SIMS-SHRIMP	Metamorphic age	Wan et al. (2009)
Meta-gabbro	Daqingshan terrane	1970–1920	SIMS-SHRIMP	Formation age of the gabbro	Wan et al. (2013)
Grt-Sil-Bt gneiss	Hujigou in Daqingshan terrane	1958 ± 10	SIMS-SHRIMP	Metamorphic age	Dong et al. (2013)
Gneissic Amp-bearing syenogranite	Wudangzhao in Daqingshan terrane	1952 ± 6	SIMS-SHRIMP	Metamorphic age	Liu et al. (2013)
Amp-bearing syneogranite	Shihao in Daqingshan terrane	1964 ± 4		Age of recrystallization immediately after formation	
Grt-bearing granite	Zhuozi in Jining terrane	1957 ± 19	LA-ICP-MS	Metamorphic age	Li et al. (2011)
Charnockite	Zhuozi in Jining terrane	1949 ± 9	LA-ICP-MS	Metamorphic age	Wang et al. (unpublished)
Gr-Grt-Sil gneiss	Huai'an Complex	1946 ± 26	SIMS-SHRIMP	Metamorphic age	Zhao et al. (2010b)
Crd-Grt-Kfs pelitic granulite		1947 ± 20			
~1.92 Ga					
Spr-bearing UHT granulite	Tuguiwula in Jining terrane	1917 ± 48	EMP monazite dating	UHT metamorphic age	Santosh et al. (2007a)
Spr-Opx-Sil-Qz-bearing UHT granulite	Tuguiwula in Jining terrane	1919 ± 10	SIMS-SHRIMP	UHT metamorphic age	Santosh et al. (2007b)
Spr-bearing UHT granulite	Tuguiwula in Jining terrane	1926 ± 13	SIMS-SHRIMP	UHT metamorphic age	Santosh et al. (2009a)
		1934 ± 16			
		1927 ± 11			
		1930 ± 11			
UHT metapelites	Helinger in Jining terrane	1913 ± 17	SIMS-SHRIMP	UHT metamorphic age	Santosh et al. (2013)
		1910 ± 18			
Grt-Sil-Bt-Pl gneiss	Qianlishan terrane	1921 ± 16	LA-ICP-MS	Post-orogenic extensional event	Yin et al. (2009)
Gabbronorite	Jining terrane	1960–1920	SIMS	Age of mafic magmatism	Peng et al. (2010)
S-type granite	Liangcheng in Jining terrane	1921 ± 16	SIMS-SHRIMP	Formation age of granite	Zhong et al. (2007)
		1908 ± 13			
S-type granite	Liangcheng in Jining terrane	1908–1918	SIMS-CAMECA	Formation age of granite	Wang et al. (unpublished)
~1.87 Ga or later					
Grt-Sil-Kfs gneiss	Huangtuyao in Jining terrane	1873 ± 32	TIMS dilution	Metamorphic age	Wu et al. (1998)
Grt-Fsp quartzite	Wulashan terrane	1801 ± 42	LA-ICP-MS	Metamorphic age	Wu et al. (2006)
Grt-Sil gneiss		1814 ± 36			
Grt-bearing arkosite		1821 ± 36			
Sil-Bt gneiss	Zhaojiayao in Jining terrane	1838 ± 16	SIMS-SHRIMP	Metamorphic age	Wan et al. (2006)
Grt-Sil gneiss	Xiabaiyao in Jining terrane	1861 ± 19			
Grt-Sil-Fsp gneiss	Huai'an Complex	1811 ± 23	LA-ICP-MS	Metamorphic age	Xia et al. (2006a)
Kfs calc-alkaline granite	Qianlishan terrane	1875 ± 19	LA-ICP-MS	Crystallization age of the granite	Yin et al. (2009)
Kfs calc-alkaline granite	Helanshan terrane	1840 ± 15	LA-ICP-MS	Crystallization age of the granite	Yin et al. (2011)
Grt-bearing S-type granite		1858 ± 23			
Grt-Sil-Crd gneiss		1865 ± 12		Tectonothermal event related to formtion of S-type granite	
Gr-Grt-Sil gneiss	Huai'an Complex	1850 ± 15	SIMS-SHRIMP	Metamorphic age	Zhao et al. (2010b)
Crd-Grt-Kfs pelitic granulite		1857 ± 16			
Charnockite	Xujiacun in Jining terrane	1858 ± 26	SIMS-SHRIMP	Metamorphic age	Santosh et al. (2013)

Note: Age interpretations follow the original authors.

1890 Ma might represent the onset of this extension/exhumation event, in the light of the preserved high metamorphic temperature and pressure (820–850 °C, some up to 950 °C; 8.5–9.5 kbar) based on the pseudosection modeling and Zr-in-rutile thermometer of Jiao et al. (2013), as well as the Ti-in-zircon temperatures in this paper. Both the associated garnet-bearing quartz-rich lenses (samples 11XSZ02-03) and the country rocks, such as the sillimanite–garnet-bearing quartzo-feldspathic gneisses (samples 11XSZ04, 06), as well as a pure quartz vein (sample 11XSZ07) and the garnet-bearing quartzo-feldspathic gneiss (sample 11XXG04) far away from the garnetite location have recorded the extension/exhumation event at ca. 1890 Ma.

The age group of ca. 1915 Ma is similar to the timing of UHT metamorphism, reported as ca. 1910–1920 Ma in the Jining terrane (Santosh et al., 2006, 2007a,b, 2009b, 2013), though Liu et al. (2013) argued that the peak UHT metamorphism might be slightly older based on the application of the Ti-in-zircon thermometer (Liu et al., 2010). Their results show that the highest Ti-in-zircon temperature 941 °C obtained from the zircon grain (with Ti concentrations of 57 ppm) associated with the Spr + Spl + Sil + Mag assemblage was slightly lower than the estimated peak metamorphic condition (>1000 °C), and most of Ti-in-zircon temperatures were around 745–870 °C. Another age group of ca. 1854 Ma is consistent with the reported age of continental collision between the Eastern and Western Blocks along the Trans-North China Orogen (Guo et al., 2001, 2005; Zhao et al., 2002, 2007, 2008a,b, 2010a; Wilde and Zhao, 2005; Kröner et al., 2006; Zhang et al., 2006, 2007, 2009; Lu et al., 2008). Alternatively, these young records may simply reflect further exhumation/extension in the Khondalite Belt.

Detrital zircon grains/cores of all the analyzed samples suggest the presence of magmatic events during Palaeoproterozoic and even up to Neoarchean, with major peaks at ca. 1932 Ma, 1964–1972 Ma, 2002–2085 Ma, and 2148–2269 Ma. These results are consistent with those reported in previous studies (Wu et al., 1998, 2006; Xia et al., 2006a,b, 2008; Wan et al., 2006, 2009, 2013; Yin et al., 2009, 2011; Zhao et al., 2010b; Li et al., 2011; Dong et al., 2013; Liu et al., 2013; Ma et al., 2012).

7.4. Implication for the tectonothermal evolution of the Khondalite Belt, North China Craton

The Khondalite Belt has generally been regarded as a collisional belt between the Yinshan and Ordos Blocks, and formed during ca. 1.95 Ga (Zhao et al., 2005). Recently, numerous metamorphic ages within the Khondalite Belt (i.e. Helanshan-Qianlishan, Daqingshan, and Jining terranes) have been reported, mainly with two peaks at 1.96–1.94 Ga and 1.88–1.82 Ga (Wu et al., 1998, 2006; Wan et al., 2006, 2009, 2013; Xia et al., 2006a; Yin et al., 2009, 2011; Dong et al., 2013; Liu et al., 2013; Ma et al., 2012; Table 2). Zhao et al. (2010b) even reported two metamorphic events at ca. 1.95 Ga and ca. 1.85 Ga from a single zircon grain in the metapelites from the Huai'an complex, a high-grade metamorphic terrane located at the conjunction of the Khondalite Belt and the Trans-North China Orogen, and they regarded these two ages as recording the timing of the two Paleoproterozoic collisional events along the Khondalite Belt and the Trans-North China Orogen, respectively.

The high metamorphic temperatures recorded by the garnetites (M1: 820–850 °C, some up to 950 °C; Jiao et al., 2013) are consistent with the regional occurrence of UHT metamorphic granulites (e.g. Santosh et al., 2006, 2007a,b; Tsunogae et al., 2011; Guo et al., 2012) and high calculated temperatures ca. 800–1000 °C obtained using the two-feldspar and Zr-in-rutile thermometers in the Khondalite Belt (Jiao and Guo, 2011; Jiao et al., 2011). The UHT metamorphism and emplacement of S-type granite began at ca. 1.92 Ga, following the collision event at ca. 1.95 Ga (Table 2) and was followed by slow extension/exhumation beginning at ca. 1.89 Ga.

8. Conclusions

Integrated accessory mineral petrography and trace element analysis and in situ, texturally controlled zircon U–Pb and monazite chemical dating of garnetite and/or associated high-grade rocks, combined with its detailed metamorphic *P–T* evolution as documented in a companion paper (Jiao et al., 2013) lead to the following conclusions for the tectonothermal history of the Khondalite Belt of the North China Craton:

(1) Zircon HREE and Y contents reflect their timing of growth in relation to poikiloblastic and corona garnet, with consistent decreases recorded from zircon present as inclusions within garnet poikiloblasts, to zircon included in the garnet rims, and to matrix zircons. Garnet poikiloblasts record rimward decreases in HREE and Y that produce bell-shaped zoning profiles compatible with Rayleigh fractionation during garnet growth. Later coronal garnet preserves a distinct chemistry (higher grossular, Cr and Li contents, lower X_{Mg}, Sm, HREE, Zn and Zr contents and weaker Eu negative anomalies) that indicates growth in a separate later event post-dating the thermal peak.
(2) Monazite chemical dating in garnetite show four major age peaks at ca. 1915 Ma, ca. 1886 Ma, ca. 1860 Ma and ca. 1820 Ma. Inclusion-type monazites generally preserve older ages than the matrix grains, but the U–Th–Pb systematics of all monazites are variably modified by the later thermal events so that the age populations distributions are skewed.
(3) The main phase of zircon growth occurred at ca. 1890 Ma. HREE distribution signatures between zircon and garnet, and Ti-in-zircon thermometer, indicate that this zircon growth was contemporaneous with the formation of poikiloblastic garnet as a peritectic phase during partial melting. This is considered to record the onset of extension and exhumation stage in the Khondalite Belt.
(4) A late-stage thermal event is recorded in zircon ages of ca. 1850 Ma and the spread of monazite ages between ca. 1860 Ma and 1820 Ma. We speculate that this may record the age of formation of coronal garnet on cooling following extension-related decompression, but the direct evidence for this in the garnetite is lacking.
(5) The Khondalite Belt of North China Craton preserves a long-lived orogenic history over a period of at least 25 Myr, from collision and associated UHT metamorphism at 1915 Ma to the onset of extension and initial exhumation at 1890 Ma.

Acknowledgments

Editor Guochun Zhao and two anonymous reviewers are thanked for their thorough review and constructive comments. We sincerely thank Chris Hayward for his help with EMP monazite dating. Xianhua Li, Qiuli Li, Yu Liu, Guoqiang Tang are thanked for their assistance during zircon SIMS dating, and Yueheng Yang and Fang Ma are thanked for their help during zircon/monazite/garnet LA-ICP-MS analyses. We also thank Zhenyu Chen for his assistance with the EMP analyses for the major elements of the garnets, and Fu Liu and Yanyan Zhou for their helps during the field work. This work was financially supported by the research Grant nos. 41023009 and 40730315 from the NSFC, and the National Basic Research Program (Grant no. 2012CB416601) of China and China Postdoctoral Science Foundation (2013M540137).

Appendix A. Supplementary data

Supplementary material related to this article can be found, in the online version, at http://dx.doi.org/10.1016/j.precamres.2013.09.008.

References

Ayers, J.C., DeLaCruz, K., Miller, C., Switzer, O., 2003. Experimental study of zircon coarsening in quartzite ± H_2O at 1.0 GPa and 1000 °C, with implications for geochronological studies of high-grade metamorphism. American Mineralogist 88, 365–376.

Bea, F., Pereira, M.D., Stroh, A., 1994. Mineral/leucosome trace-element partitioning in a peraluminous migmatite (a laser ablation-ICP-MS study). Chemical Geology 117, 291–312.

Bea, F., Montero, P., Garuti, G., Zacharini, F., 1997. Pressure-dependence of rare earth element distribution in amphibolite- and granulite-grade garnets. A LA-ICP-MS study. Geostandards Newsletter – The Journal of Geostandards and Geoanalysis 21, 253–270.

Berry, R.F., Chmielowski, R.M., Steele, D.A., Meffre, S., 2007. Chemical U–Th–Pb monazite dating of the Cambrian Tyennan Orogeny, Tasmania. Australian Journal of Earth Sciences 54, 757–771.

Bingen, B., Austrheim, H., Whitehouse, M., 2001. Ilmenite as a source for zirconium during high-grade metamorphism? Textural evidence from the Caledonides of western Norway and implications for zircon geochronology. Journal of Petrology 42, 355–375.

Bingen, B., Austrheim, H., Whitehouse, M.J., Davis, W.J., 2004. Trace element signature and U–Pb geochronology of eclogite-facies zircon, Bergen Arcs, Caledonides of W Norway. Contributions to Mineralogy and Petrology 147, 671–683.

Braun, I., Montel, J.M., Nicollet, C., 1998. Electron microprobe dating of monazites from high-grade gneisses and pegmatites of the Kerala Khondalite Belt, southern India. Chemical Geology 146, 65–85.

Carlson, W.D., 2012. Rates and mechanism of Y, REE, and Cr diffusion in garnet. American Mineralogist 97, 1598–1618.

Cherniak, D.J., Watson, E.B., 2001. Pb diffusion in zircon. Chemical Geology 172, 5–24.

Cherniak, D.J., Watson, E.B., Grove, M., Harrison, T.M., 2004. Pb diffusion in monazite: a combined RBS/SIMS study. Geochimica et Cosmochimica Acta 68, 829–840.

Clark, C., Collins, A.S., Santosh, M., Taylor, R., Wade, B.P., 2009. The *P–T–t* architecture of a Gondwanan suture: REE, U–Pb and Ti-in-zircon thermometric constraints from the Palghat Cauvery shear system, South India. Precambrian Research 174, 129–144.

Cocherie, A., Albarede, F., 2001. An improved U–Th–Pb age calculation for electron microprobe dating of monazite. Geochimica et Cosmochimica Acta 65, 4509–4522.

Cocherie, A., Legendre, O., Peucat, J.J., Kouamelan, A.N., 1998. Geochronology of polygenetic monazites constrained by in situ electron microprobe Th–U total lead determination: implications for lead behaviour in monazite. Geochimica et Cosmochimica Acta 62, 2475–2497.

Condie, K.C., Boryta, M.D., Liu, J.Z., Qian, X.L., 1992. The origin of khondalites: geochemical evidence from the Archean to early Proterozoic granulite belt in the North China cration. Precambrian Research 59, 207–223.

Crowley, J.L., Ghent, E.D., 1999. An electron microprobe study of the U–Th–Pb systematics of metamorphosed monazite: the role of Ph diffusion versus overgrowth and recrystallization. Chemical Geology 157, 285–302.

Degeling, H., Eggins, S., Ellis, D.J., 2001. Zr budgets for metamorphic reactions, and the formation of zircon from garnet breakdown. Mineralogical Magazine 65, 749–758.

Dong, C., Wan, Y., Xu, Z., Liu, D., Yang, Z., Ma, M., Xie, H., 2013. SHRIMP zircon U–Pb dating of late Paleoproterozoic kondalites in the Daqing Mountains area on the North China Craton. Science China (Earth Sciences) 56, 115–125.

Fitzsimons, I.C.W., Kinny, P.D., Wetherley, S., Hollingsworth, D.A., 2005. Bulk chemical control on metamorphic monazite growth in pelitic schists and implications for U–Pb age data. Journal of Metamorphic Geology 23, 261–277.

Fraser, G., Ellis, D., Eggins, S., 1997. Zirconium abundance in granulite-facies minerals, with implications for zircon geochronology in high-grade rocks. Geology 25, 607–610.

Guo, J.H., Wang, S.S., Sang, H.Q., Zhai, M.G., 2001a. ^{40}Ar–^{39}Ar age spectra of garnet porphyroblast: implications for metamorphic age of high-pressure granulite in the North China Craton. Acta Petrologica Sinica 17, 436–442.

Guo, J.H., Sun, M., Chen, F.K., Zhai, M.G., 2005. Sm–Nd and SHRIMP U–Pb zircon geochronology of high-pressure granulites in the Sanggan area, North China Craton: timing of Paleoproterozoic continental collision. Journal of Asian Earth Sciences 24, 629–642.

Guo, J., Peng, P., Chen, Y., Jiao, S., Windley, B.F., 2012. UHT sapphirine granulite metamorphism at 1.93–1.92 Ga caused by gabbronorite intrusions: implications for tectonic evolution of the northern margin of the North China Craton. Precambrian Research 222–223, 124–142.

Harley, S.L., Kinny, P.D., Snape, I., Black, L.P., 2001. zircon chemistry and the definition of events in Archaean granulite terrains. In: Cassidy, K.F., Dunphy, J.M., van Kranendonk, M.J. (Eds.), Extended Abstracts of 4th International Archaean Symposium. AGSO-Geoscience Australia Record 2001/37. Canberra, pp. 511–513.

Harley, S.L., Kelly, N.M., Moller, A., 2007. Zircon behaviour and the thermal histories of mountain chains. Elements 3, 25–30.

Hermann, J., Rubatto, D., 2003. Relating zircon and monazite domains to garnet growth zones: age and duration of granulite facies metamorphism in the Val Malenco lower crust. Journal of Metamorphic Geology 21, 833–852.

Högdahl, K., Majka, J., Sjöström, H., Nilsson, K., Claesson, S., Konečný, P., 2012. Reactive monazite and robust zircon growth in diatexites and leucogranites from a hot, slowly cooled orogen: implications for the Palaeoproterozoic tectonic evolution of the central Fennoscandian Shield, Sweden. Contributions to Mineralogy and Petrology 163, 167–188.

Hollister, L.S., 1966. Garnet zoning: an interpretation based on the Rayleigh fractionation model. Science 154, 1647–1651.

Hoskin, P.W.O., Black, L.P., 2000. Metamorphic zircon formation by solid-state recrystallization of protolith igneous zircon. Journal of Metamorphic Geology 18, 423–439.

Hu, J.M., Liu, X.S., Li, Z.H., Zhao, Y., Zhang, S.H, Liu, X.C., Qu, H.J., Chen, H., 2013. SHRIMP U–Pb zircon dating of the Ordos Basin basement and its tectonic significance. Chinese Science Bulletin 58, 118–127.

Jiao, S.J., Guo, J.H., 2011. Application of the two-feldspar geothermometer to ultrahigh-temperature (UHT) rocks in the Khondalite belt, North China craton and its implications. American Mineralogist 96, 250–260.

Jiao, S., Guo, J., Mao, Q., Zhao, R., 2011. Application of Zr-in-rutile thermometry: a case study from ultrahigh-temperature granulites of the Khondalite belt, North China Craton. Contributions to Mineralogy and Petrology 162, 379–393.

Jiao, S., Guo, J., Harley, S.L., Windley, B.F., 2013. New constraints from garnetite on the *P–T* path of the Khondalite Belt: implications for the tectonic evolution of the North China Craton. Journal of Petrology 54, 1725–1758.

Kawakami, T., Yamaguchi, I., Miyake, A., Shibata, T., Maki, K., Yokoyama, T., Hirata, T., 2013. Behavior of zircon in the upper-amphibolite to granulite facies schist/migmatite transition, Ryoke metamorphic belt, SW Japan: constraints from the melt inclusions in zircon. Contributions to Mineralogy and Petrology 165, 575–591.

Kelly, N.M., Clarke, G.L., Harley, S.L., 2006. Monazite behaviour and age significance in poly-metamorphic high-grade terrains: a case study from the western Musgrave Block, central Australia. Lithos 88, 100–134.

Kelsey, D.E., Powell, R., Wilson, C.J.L., Steele, D.A., 2003. (Th + U)-Pb monazite ages from Al–Mg-rich metapelites, Rauer Group, east Antarctica. Contributions to Mineralogy and Petrology 146, 326–340.

Kelsey, D.E., Powell, R., 2011. Progress in linking accessory mineral growth and breakdown to major mineral evolution in metamorphic rocks: a thermodynamic approach in the Na_2O–CaO–K_2O–FeO–MgO–Al_2O_3–SiO_2–H_2O–TiO_2–ZrO_2 system. Journal of Metamorphic Geology 29, 151–166.

Kröner, A., Wilde, S.A., Zhao, G.C., O'Brien, P.J., Sun, M., Liu, D.Y., Wan, Y.S., Liu, S.W., Guo, J.H., 2006. Zircon geochronology and metamorphic evolution of mafic dykes in the Hengshan Complex of northern China: evidence for late Palaeoproterozoic extension and subsequent high-pressure metamorphism in the North China Craton. Precambrian Research 146, 45–67.

Li, X.H., Liu, Y., Li, Q.L., Guo, C.H., Chamberlain, K.R., 2009. Precise determination of Phanerozoic zircon Pb/Pb age by multicollector SIMS without external standardization. Geochemistry Geophysics Geosystems 10, http://dx.doi.org/10.1029/2009gc002400.

Li, Q.L., Li, X.H., Liu, Y., Tang, G.Q., Yang, J.H., Zhu, W.G., 2010a. Precise U–Pb and Pb–Pb dating of Phanerozoic baddeleyite by SIMS with oxygen flooding technique. Journal of Analytical Atomic Spectrometry 25, 1107–1113.

Li, S.Z., Zhao, G.C., Zhang, J., Sun, M., Zhang, G.W., Luo, D., 2010b. Deformational history of the Hengshan-Wutai-Fuping belt: implications for the evolution of the Trans-North China Orogen. Gondwana Research 18, 611–631.

Li, X.P., Yang, Z.Y., Zhao, G.C., Grapes, R., Guo, J.H., 2011. Geochronology of khondalite-series rocks of the Jining complex: confirmation of depositional age and tectonometamorphic evolution of the North China craton. International Geology Review 53, 1194–1211.

Liu, S.W., Zhao, G.C., Wilde, S.A., Shu, G.M., Sun, M., Li, Q.G., Tian, W., Zhang, J., 2006. Th–U–Pb monazite geochronology of the Lüliang and Wutai Complexes: constraints on the tectonothermal evolution of the Trans-North China Orogen. Precambrian Research 148, 205–224.

Liu, S.J., Li, J.H., Santosh, M., 2010. First application of the revised Ti-in-zircon geothermometer to Paleoproterozoic ultrahigh-temperature granulites of Tuguiwula, Inner Mongolia, North China Craton. Contributions to Mineralogy and Petrology 159, 225–235.

Liu, S., Dong, C., Xu, Z., Santosh, M., Ma, M., Xie, H., Liu, D., Wan, Y., 2013. Palaeoproterozoic episodic magmatism and high-grade metamorphism in the North China Craton: evidence from SHRIMP zircon dating of magmatic suites in the Daqingshan area. Geological Journal 48, 429–455.

Lu, L.Z., Jin, S.Q., Xu, X.C., Liu, F.L., 1992. The Genesis of Early Precambrian Khondalite Series in Southeastern Inner Mongolia and its Potential Mineral Resources. Jilin Scientific and Technical Publishing House, Changchun.

Lu, L.Z., Xu, X.C., Liu, F.L., 1996. The Precambrian Khondalite Series of Northern China. Changchun Publishing House, Changchun.

Lu, S.N., Zhao, G.C., Wang, H.C., Hao, G.J., 2008. Precambrian metamorphic basement and sedimentary cover of the North China Craton: a review. Precambrian Research 160, 77–93.

Ludwig, K.R., 2001. Users manual for Isoplot/Ex rev. 2.49. Berkeley Geochronology Centre Special Publication No. 1a, 56 pp.

Ma, M., Wan, Y., Santosh, M., Xu, Z., Xie, H., Dong, C., Liu, D., Guo, C., 2012. Decoding multiple tectonothermal events in zircons from single rock samples: SHRIMP zircon U–Pb data from the late Neoarchean rocks of Daqingshan, North China Craton. Gondwana Research 22, 810–827.

Montel, J.M., Foret, S., Veschambre, M., Nicollet, C., Provost, A., 1996. Electron microprobe dating of monazite. Chemical Geology 131, 37–53.
Möller, A., O'Brien, P.J., Kennedy, A., Kroner, A., 2002. Polyphase zircon in ultrahigh-temperature granulites (Rogaland, SW Norway): constraints for Pb diffusion in zircon. Journal of Metamorphic Geology 20, 727–740.
Nemchin, A.A., Giannini, L.M., Bodorkos, S., Oliver, N.H.S., 2001. Ostwald ripening as a possible mechanism for zircon overgrowth formation during anatexis: theoretical constraints, a numerical model, and its application to pelitic migmatites of the Tickalara Metamorphics, northwestern Australia. Geochimica et Cosmochimica Acta 65, 2771–2788.
Orejana, D., Villaseca, C., Armstrong, R.A., Jeffries, T.E., 2011. Geochronology and trace element chemistry of zircon and garnet from granulite xenoliths: constraints on the tectonothermal evolution of the lower crust under central Spain. Lithos 124, 103–116.
Otamendi, J.E., de la Rosa, J.D., Patiño Douce, A.E., Castro, A., 2002. Rayleigh fractionation of heavy rare earths and yttrium during metamorphic garnet growth. Geology 30, 159–162.
Pearce, N.J.G., Perkins, W.T., Westgate, J.A., Gorton, M.P., Jackson, S.E., Neal, C.R., Chenery, S.P., 1997. A compilation of new and published major and trace element data for NIST SRM 610 and NIST SRM 612 glass reference materials. Geostandards Newsletter – The Journal of Geostandards and Geoanalysis 21, 115–144.
Peng, P., Guo, J.H., Zhai, M.G., Bleeker, W., 2010. Paleoproterozoic gabbronoritic and granitic magmatism in the northern margin of the North China craton: evidence of crust-mantle interaction. Precambrian Research 183, 635–659.
Roberts, M.P., Finger, F., 1997. Do U–Pb zircon ages from granulites reflect peak metamorphic conditions? Geology 25, 319–322.
Rubatto, D., 2002. Zircon trace element geochemistry: partitioning with garnet and the link between U–Pb ages and metamorphism. Chemical Geology 184, 123–138.
Rubatto, D., Hermann, J., 2007a. Experimental zircon/melt and zircon/garnet trace element partitioning and implications for the geochronology of crustal rocks. Chemical Geology 241, 38–61.
Rubatto, D., Hermann, J., 2007b. Zircon behaviour in deeply subducted rocks. Elements 3, 31–35.
Rubatto, D., Williams, I.S., Buick, I.S., 2001. Zircon and monazite response to prograde metamorphism in the Reynolds Range, central Australia. Contributions to Mineralogy and Petrology 140, 458–468.
Rubatto, D., Hermann, J., Buick, I.S., 2006. Temperature and bulk composition control on the growth of monazite and zircon during low-pressure anatexis (Mount Stafford, Central Australia). Journal of Petrology 47, 1973–1996.
Santosh, M., 2010. Assembling North China Craton within the Columbia supercontinent: the role of double-sided subduction. Precambrian Research 178, 149–167.
Santosh, M., Sajeev, K., Li, J.H., 2006. Extreme crustal metamorphism during Columbia supercontinent assembly: evidence from North China Craton. Gondwana Research 10, 256–266.
Santosh, M., Tsunogae, T., Li, J.H., Liu, S.J., 2007a. Discovery of sapphirine-bearing Mg–Al granulites in the North China Craton: implications for Paleoproterozoic ultrahigh temperature metamorphism. Gondwana Research 11, 263–285.
Santosh, M., Wilde, S.A., Li, J.H., 2007b. Timing of Paleoproterozoic ultrahigh-temperature metamorphism in the North China Craton: evidence from SHRIMP U–Pb zircon geochronology. Precambrian Research 159, 178–196.
Santosh, M., Sajeev, K., Li, J.H., Liu, S.J., Itaya, T., 2009a. Counterclockwise exhumation of a hot orogen: the Paleoproterozoic ultrahigh-temperature granulites in the North China Craton. Lithos 110, 140–152.
Santosh, M., Wan, Y.S., Liu, D.Y., Dong, C.Y., Li, J.H., 2009b. Anatomy of zircons from an ultrahot Orogen: the amalgamation of the North China Craton within the Supercontinent Columbia. Journal of Geology 117, 429–443.
Santosh, M., Liu, D., Shi, Y., Liu, S.J., 2013. Paleoproterozoic accretionary orogenesis in the North China Craton: a SHRIMP zircon study. Precambrian Research 227, 29–54.
Schaltegger, U., Fanning, C.M., Gunther, D., Maurin, J.C., Schulmann, K., Gebauer, D., 1999. Growth, annealing and recrystallization of zircon and preservation of monazite in high-grade metamorphism: conventional and in-situ U–Pb isotope, cathodoluminescence and microchemical evidence. Contributions to Mineralogy and Petrology 134, 186–201.
Spear, F.S., Kohn, M.J., 1996. Trace element zoning in garnet as a monitor of crustal melting. Geology 24, 1099–1102.
Stacey, J.S., Kramers, J.D., 1975. Approximation of terrestrial lead isotope evolution by a 2-stage model. Earth and Planetary Science Letters 26, 207–221.
Sun, S.-s., McDonough, W.F., 1989. Chemical and isotopic systematics of oceanic basalts: implications for mantle composition and processes. Geological Society, London, Special Publications 42, 313–345.
Tirone, M., Ganguly, J., Dohmen, R., Langenhorst, F., Hervig, R., Becker, H.W., 2005. Rare earth diffusion kinetics in garnet: experimental studies and applications. Geochimica et Cosmochimica Acta 69, 2385–2398.
Tsunogae, T., Liu, S.J., Santosh, M., Shimizu, H., Li, J.H., 2011. Ultrahigh-temperature metamorphism in Daqingshan, Inner Mongolia Suture Zone, North China Craton. Gondwana Research 20, 36–47.
Van Orman, J.A., Grove, T.L., Shimizu, N., Layne, G.D., 2002. Rare earth element diffusion in a natural pyrope single crystal at 2.8 GPa. Contributions to Mineralogy and Petrology 142, 416–424.
Vavra, G., Schmid, R., Gebauer, D., 1999. Internal morphology, habit and U–Th–Pb microanalysis of amphibolite-to-granulite facies zircons: geochronology of the Ivrea Zone (Southern Alps). Contributions to Mineralogy and Petrology 134, 380–404.
Wan, Y.S., Song, B., Liu, D.Y., Wilde, S.A., Wu, J.S., Shi, Y.R., Yin, X.Y., Zhou, H.Y., 2006. SHRIMP U–Pb zircon geochronology of Palaeoproterozoic metasedimentary rocks in the North China Craton: evidence for a major Late Palaeoproterozoic tectonothermal event. Precambrian Research 149, 249–271.
Wan, Y., Liu, D., Xu, Z., Dong, C., Wang, Z., Zhou, H., Yang, Z., Liu, Z., Wu, J., 2008. Paleoproterozoic crustally derived carbonate-rich magmatic rocks from the Daqinshan area, North China Craton: geological, petrographical, geochronological and geochemical (Hf, Nd, O and C) evidence. American Journal of Science 308, 351–378.
Wan, Y., Liu, D., Dong, C., Xu, Z., Wang, Z., Wilde, S.A., Yang, Y., Liu, Z., Zhou, H., 2009. The Precambrian Khondalite Belt in the Daqingshan area, North China Craton: evidence for multiple metamorphic events in the Palaeoproterozoic era. Geological Society, London, Special Publications 323, 73–97.
Wan, Y., Xu, Z., Dong, C., Nutman, A., Ma, M., Xie, H., Liu, S., Liu, D., Wang, H., Cu, H., 2013. Episodic Paleoproterozoic (~2.45, ~1.95 and ~1.85 Ga) mafic magmatism and associated high temperature metamorphism in the Daqingshan area, North China Craton: SHRIMP zircon U–Pb dating and whole-rock geochemistry. Precambrian Research 224, 71–93.
Watson, E.B., 1996. Dissolution, growth and survival of zircons during crustal fusion: kinetic principles, geological models and implications for isotopic inheritance. Geological Society of America Special Papers 315, 43–56.
Watson, E.B., Wark, D.A., Thomas, J.B., 2006. Crystallization thermometers for zircon and rutile. Contributions to Mineralogy and Petrology 151, 413–433.
Whitehouse, M.J., Platt, J.P., 2003. Dating high-grade metamorphism – constraints from rare-earth elements in zircon and garnet. Contributions to Mineralogy and Petrology 145, 61–74.
Whitney, D.L., Evans, B.W., 2010. Abbreviations for names of rock-forming minerals. American Mineralogist 95, 185–187.
Wiedenbeck, M., AllÉ, P., Corfu, F., Griffin, W.L., Meier, M., Oberli, F., Quadt, A.V., Roddick, J.C., Spiegel, W., 1995. Three natureal zircon standards for U–Th–Pb, Lu-Hf, trace element and REE analyses. Geostandards Newsletter – The Journal of Geostandards and Geoanalysis 19, 1–23.
Wilde, S.A., Zhao, G.C., 2005. Archean to Paleoproterozoic evolution of the North China Craton. Journal of Asian Earth Sciences 24, 519–522.
Wu, C.H., Li, H.M., Zhong, C.T., Chen, Q.A., 1998. The ages of zircon and rutile (cooling) from khondalite in Huangtuyao, Inner Mongolia. Geological Review 44, 618–626.
Wu, C.H., Sun, M., Li, H.M., Zhao, G.C., Xia, X.P., 2006. LA-ICP-MS U–Pb zircon ages of the khondalites from the Wulashan and Jining high-grade terrain in northern margin of the North China Craton: constraints on sedimentary age of the khondalite. Acta Petrologica Sinica 22, 2639–2654.
Xia, X.P., Sun, M., Zhao, G.C., Luo, Y., 2006a. LA-ICP-MS U–Pb geochronology of detrital zircons from the Jining Complex, North China Craton and its tectonic significance. Precambrian Research 144, 199–212.
Xia, X.P., Sun, M., Zhao, G.C., Wu, F.Y., Xu, P., Zhang, J.H., Luo, Y., 2006b. U–Pb and Hf isotopic study of detrital zircons from the Wulashan khondalites: constraints on the evolution of the Ordos Terrane, Western Block of the North China Craton. Earth and Planetary Science Letters 241, 581–593.
Xia, X.P., Sun, M., Zhao, G.C., Wu, F.Y., Xu, P., Zhang, J., He, Y.H., 2008. Paleoproterozoic crustal growth in the Western Block of the North China Craton: evidence from detrital zircon Hf and whole rock Sr–Nd isotopic compositions of the Khondalites from the Jining Complex. American Journal of Science 308, 304–327.
Xiao, L.L., Wu, C.M., Zhao, G.C., Guo, J.H., Ren, L.D., 2011. Metamorphic *P–T* paths of the Zanhuang amphibolites and metapelites: constraints on the tectonic evolution of the Paleoproterozoic Trans-North China Orogen. International Journal of Earth Sciences 100, 717–739.
Yin, C.Q., Zhao, G.C., Sun, M., Xia, X.P., Wei, C.J., Zhou, X.W., Leung, W.H., 2009. LA-ICP-MS U–Pb zircon ages of the Qianlishan complex: constrains on the evolution of the Khondalite Belt in the Western Block of the North China Craton. Precambrian Research 174, 78–94.
Yin, C.Q., Zhao, G.C., Guo, J.H., Sun, M., Xia, X.P., Zhou, X.W., Liu, C.H., 2011. U–Pb and Hf isotopic study of zircons of the Helanshan complex: constrains on the evolution of the Khondalite Belt in the Western Block of the North China Craton. Lithos 122, 25–38.
Zhang, J., Zhao, G.C., Sun, M., Wilde, S.A., Li, S.Z., Liu, S.W., 2006. High-pressure mafic granulites in the Trans-North China Orogen: tectonic significance and age. Gondwana Research 9, 349–362.
Zhang, J., Zhao, G.C., Li, S.Z., Sun, M., Liu, S.W., Wilde, S.A., Kröner, A., Yin, C.Q., 2007. Deformation history of the Hengshan Complex: implications for the tectonic evolution of the Trans-North China Orogen. Journal of Structural Geology 29, 933–949.
Zhang, J., Zhao, G.C., Li, S.Z., Sun, M., Wilde, S.A., Liu, S.W., Yin, C.Q., 2009. Polyphase deformation of the Fuping Complex, Trans-North China Orogen: structures, SHRIMP U–Pb zircon ages and tectonic implications. Journal of Structural Geology 31, 177–193.
Zhao, G.C., Guo, J.H., 2012. Precambrian Geology of China: preface. Precambrian Research 222–223, 1–12.
Zhao, G.C., Cawood, P.A., 2012. Precambrian Geology of China. Precambrian Research 222–223, 13–54.
Zhao, G.C., Sun, M., Wilde, S.A., Li, S.Z., Liu, S.W., Zhang, J., 2006. Composite nature of the North China Granulite-Facies Belt: tectonothermal and geochronological constraints. Gondwana Research 9, 337–348.
Zhao, G., Zhai, M., 2013. Lithotectonic elements of Precambrian basement in the North China Craton: review and tectonic implications. Gondwana Research 23, 1207–1240.

Zhao, G.C., Wilde, S.A., Cawood, P.A., Lu, L.Z., 1999. Tectonothermal history of the basement rocks in the western zone of the North China Craton and its tectonic implications. Tectonophysics 310, 37–53.

Zhao, G.C., Wilde, S.A., Cawood, P.A., Sun, M., 2001. Archean blocks and their boundaries in the North China Craton: lithological, geochemical, structural and *P–T* path constraints and tectonic evolution. Precambrian Research 107, 45–73.

Zhao, G.C., Wilde, S.A., Cawood, P.A., Sun, M., 2002. SHRIMP U–Pb zircon ages of the Fuping Complex: implications for Late Archean to Paleoproterozoic accretion and assembly of the North China Craton. American Journal of Science 302, 191–226.

Zhao, G.C., Sun, M., Wilde, S.A., 2003. Major tectonic units of the North China Craton and their Paleoproterozoic assembly. Science in China Series D – Earth Sciences 46, 23–38.

Zhao, G.C., Sun, M., Wilde, S.A., Li, S.Z., 2005. Late Archean to Paleoproterozoic evolution of the North China Craton: key issues revisited. Precambrian Research 136, 177–202.

Zhao, G.C., Kroener, A., Wilde, S.A., Sun, M., Li, S.Z., Li, X.P., Zhang, J., Xia, X.P., He, Y.H., 2007. Lithotectonic elements and geological events in the Hengshan-Wutai-Fuping belt: a synthesis and implications for the evolution of the Trans-North China Orogen. Geological Magazine 144, 753–775.

Zhao, G.C., Wilde, S.A., Sun, M., Guo, J.H., Kroener, A., Li, S.Z., Li, X.P., Zhang, J., 2008a. SHRIMP U–Pb zircon geochronology of the Huai'an Complex: constraints on late Archean to Paleoproterozoic magmatic and metamorphic events in the Trans-North China Orogen. American Journal of Science 308, 270–303.

Zhao, G.C., Wilde, S.A., Sun, M., Li, S.Z., Li, X.P., Zhang, J., 2008b. SHRIMP U–Pb zircon ages of granitoid rocks in the Lüliang complex: implications for the accretion and evolution of the Trans-North China Orogen. Precambrian Research 160, 213–226.

Zhao, G., Yin, C., Guo, J., Sun, M., Li, S., Li, X., Wu, C., Liu, C., 2010a. Metamorphism of the Lüliang amphibolite: implications for the tectonic evolution of the North China Craton. American Journal of Science 310, 1480–1502.

Zhao, G.C., Wilde, S.A., Guo, J.H., Cawood, P.A., Sun, M., Li, X.P., 2010b. Single zircon grains record two Paleoproterozoic collisional events in the North China Craton. Precambrian Research 177, 266–276.

Zheng, Y.F., Xiao, W.J., Zhao, G.C., 2013. Introduction to tectonics of China. Gondwana Research 23, 1189–1206.

Zhong, C.T., Deng, J.F., Wan, Y.S., Mao, D.B., Li, H.M., 2007. Magma recording of Paleoproterozoic orogeny in central segment of northern margin of North China Cration: geochemical characteristics and zircon SHRIMP dating of S-type granitoids. Geochimica 36, 633–637.